J. Fluid Mech. (2010), *vol.* 662, *pp.* 232–259. © Cambridge University Press 2010
doi:10.1017/S0022112010003174

Circular cylinder vortex-synchronization control with a synthetic jet positioned at the rear stagnation point

LI HAO FENG AND JIN JUN WANG†

Fluid Mechanics Institute, Beijing University of Aeronautics and Astronautics and Fluid Mechanics Key Laboratory of Education Ministry, Beijing 100191, China

(Received 4 November 2009; revised 8 June 2010; accepted 8 June 2010; first published online 25 August 2010)

The flow over a circular cylinder controlled by a two-dimensional synthetic jet positioned at the mean rear stagnation point has been experimentally investigated in a water channel at the cylinder Reynolds number $Re = 950$. This is an innovative arrangement and the particle-image-velocimetry measurement indicates that it can lead to a novel and interesting phenomenon. The synthetic-jet vortex pairs induced near the exit convect downstream and interact with the vorticity shear layers behind both sides of the cylinder, resulting in the formation of new induced wake vortices. The present vortex synchronization occurs when the excitation frequency of the synthetic jet is between 1.67 and 5.00 times the natural shedding frequency at the dimensionless stroke length 99.5. However, it is suggested that the strength of the synthetic-jet vortex pair plays a more essential role in the occurrence of vortex synchronization than the excitation frequency. In addition, the wake-vortex shedding is converted into a symmetric mode from its original antisymmetric mode. The symmetric shedding mode weakens the interaction between the upper and lower wake vortices, resulting in a decrease in the turbulent kinetic energy produced by them. It also has a significant influence on the global flow field, including the velocity fluctuations, Reynolds stresses and flow topology. However, their distributions are still dominated by the large-scale coherent structures.

Key words: turbulence control, vortex interactions, vortex shedding

1. Introduction

Vortex shedding over a bluff body usually causes serious structural vibrations, acoustic noise and resonance, enhanced mixing and significant increases in the mean drag and lift fluctuations (Choi, Jeon & Kim 2008). Therefore, effective control of vortex shedding is important in engineering applications, which can successfully lead to separation delay, drag reduction, and reduction of vibration and noise. The related control methods can be categorized into passive and active techniques, such as splitter plate, roughness, geometric modification, base bleed, oscillation, rotation, acoustic excitation, plasma and synthetic jet methods. As a typical bluff body, the circular cylinder flow control is regarded as an important aspect of these investigations. There are many common features resulting from the interactions between the external perturbations and the flow around the circular cylinder: for example, the

† Email address for correspondence: jjwang@buaa.edu.cn

vortex-shedding frequency can be affected by the perturbations. This may mainly result in two phenomena. One is that the imposed perturbations could suppress the Kármán-vortex shedding. For instance, Huang (1995, 1996) acoustically controlled a circular cylinder by two loudspeakers connected to each end of the cylinder and proved its ability to suppress the natural predominant frequency of the Kármán vortex when the jet was positioned at $\alpha = 80°$; recently, Dipankar, Sengupta & Talla (2007) found that the vortex shedding behind a cylinder could be suppressed by placing another small cylinder behind it, which also led to a reduction in drag. The other is the synchronization of the vortex-shedding frequency with that of the perturbations, commonly termed as vortex lock-on (Griffin & Hall 1991) or vortex synchronization (Kim *et al.* 2009), which has already drawn much attention in the review paper by Griffin & Hall (1991).

According to the previous investigations, there are mainly two methods that could result in vortex synchronization: (i) a circular cylinder oscillating with prescribed motions, including transverse motion (e.g. Stansby 1976; Mahir & Rockwell 1996; Blackburn & Henderson 1999; Krishnamoorthy, Price & Païdoussis 2001) and streamwise motion (e.g. Griffin & Ramberg 1976; Ongoren & Rockwell 1988; Nishihara, Kaneko & Watanabe 2005), and (ii) perturbations imposed on the free stream, including transverse perturbations (e.g. Hall, Ziada & Weaver 2003) and streamwise perturbations (e.g. Barbi *et al.* 1986; Armstrong, Barnes & Grant 1986, 1987; Hall & Griffin 1993; Konstantinidis, Balabani & Yianneskis 2003, 2005*a*,*b*; Konstantinidis & Balabani 2007, 2008; Jarża & Podolski 2004; Kim, Yoo & Sung 2006; Kim *et al.* 2009). These numerous methods are all conducted by the interactions between the periodic external perturbations and the intrinsic instability of the wake vortex, which can be considered as a function of the excitation frequency and amplitude (Konstantinidis & Balabani 2007).

The following primary conclusions can be made by the statistical analysis of the above investigations. (i) The vortex-synchronization regime is related to both the excitation frequency and amplitude, and the fundamental trend is that a higher excitation amplitude can induce a much larger vortex-synchronization regime. (ii) The range of the excitation frequency resulting in vortex synchronization is usually around $f_e/f_o = 1$ or $f_e/f_o = 2$, with the minimum $f_e/f_o = 0.67$ (Stansby 1976) and the maximum $f_e/f_o = 2.5$ (Griffin & Ramberg 1976) in these works. (iii) Vortex-synchronization phenomena can be categorized into two groups: vortex synchronization at the excitation frequency and at the subharmonic excitation frequency. Transverse oscillation and transverse perturbation flow may result in vortex synchronization at the excitation frequency, while streamwise oscillation and streamwise perturbation flow usually result in vortex synchronization at the subharmonic excitation frequency. (iv) The excitation amplitude needed to induce vortex synchronization differs between the two control methods. The cylinder oscillation amplitude A, normalized by the cylinder diameter D, is usually of the order of 10^{-1}, while the velocity oscillation amplitude Δu, normalized by the cylinder diameter D together with the excitation frequency f_e in the form of $\Delta u/\pi f_e D$, is usually of the order of 10^{-2}. Hall *et al.* (2003) compared the perturbation flow to the forced oscillation and indicated that the amplitude required to produce vortex synchronization by the former was roughly an order of magnitude lower than the latter, suggesting that the vortex shedding was much more sensitive to the perturbation flow than to the cylinder motion.

The wake-vortex-shedding mode might also change due to the external perturbations. Based on the temporal and spatial distributions, Ongoren & Rockwell

(1988) indicated that modes of vortex formation could be categorized into two basic groups: a symmetric mode denoted as S, and an antisymmetric mode denoted as A, which appeared in four forms, A-I, A-II, A-III and A-IV. For the symmetric mode, a pair of vortices was shedding in phase from both sides of the circular cylinder during one oscillation cycle. In the case of the A-I mode, there was alternate out-of-phase shedding of vortices from either side of the cylinder over one oscillation cycle. For modes A-II–A-IV, the period of the vortex pattern is twice that of the classical A-I mode. Xu, Zhou & Wang (2006) validated the existence of S, A-I, A-III and A-IV modes. Furthermore, they observed a new symmetric shedding mode, named S-II, experimentally for the first time. It consisted of two rows of binary vortices symmetrically arranged about the centreline of the wake. Each binary vortex contained two counter-rotating vortices shedding from the same side of the cylinder. Lucor & Karniadakis (2004) have also suggested that the dominant vortex patterns of an oscillation circular cylinder near the fundamental synchronization region are 2S, 2P and P+S, corresponding to the A-I, A-IV and A-III modes mentioned by Ongoren & Rockwell (1988) and Xu *et al.* (2006), respectively. Adopting this classification, the standard Kármán-vortex shedding is equivalent to an A-I mode (or 2S mode). Besides, the symmetric shedding mode is potentially of engineering significance and should be given special attention, since this flow structure leads to zero mean and fluctuating lift on the cylinder (Xu *et al.* 2006). Barbi *et al.* (1986), Ongoren & Rockwell (1988), Detemple-Laake & Eckelmann (1989), Zhou & Graham (2000), Gau, Wu & Su (2001), Liu & Fu (2003), Jauvtis & Williamson (2004), Nishihara *et al.* (2005), Xu *et al.* (2006), Konstantinidis & Balabani (2007) and Jukes & Choi (2009) all observed the existence of the symmetric vortex-shedding mode by means of cylinder oscillations, free-stream perturbations or symmetric perturbations imposed at both top and bottom separation points. For more details about the symmetric shedding mode, refer to the summary of Konstantinidis & Balabani (2007).

Most of the cylinder flow-control methods mentioned above belong to traditional techniques. In recent decades, the synthetic-jet flow-control technique has drawn much attention because of its great advantages (Smith & Glezer 1998; Shuster & Smith 2007). The synthetic jet can be further miniaturized based on micro-electro-mechanical systems (MEMS) technology with internal, accurate, feedback and real-time control. It has been applied widely in various fields (Glezer & Amitay 2002; Zhang, Wang & Feng 2008). One of these is to control the circular cylinder flow separation. Many previous investigations have proved that the synthetic jet can effectively delay the circular cylinder separation, make the separation region diminish or even completely disappear, and lead to a drag reduction. Some representative works are summarized in table 1. Among these investigations, the synthetic-jet exit was usually positioned near the separation point, whereas Amitay *et al.* (1997), Tensi *et al.* (2002) and Feng, Wang & Xu (2008) also pointed out that the synthetic jet could effectively control flow separation around a circular cylinder when positioned at the mean rear stagnation point.

There are some other circular cylinder control techniques based on the rear stagnation point, such as the base bleed and splitter plate methods. Tan, Wang & Li (2001) indicated that the base bleed could change the wake of a hollow cylinder. Fu & Rockwell (2005) found that vortex formation in the near wake of shallow flow past a circular cylinder could be substantially delayed by base bleed through a very narrow slot. The wake structures associated with this delay changed dramatically with the dimensionless momentum coefficient of the slot bleed. Baek & Karniadakis (2009) indicated that a slot of sufficiently large width positioned in a modified cylinder could cause a strong jet flow into the near wake, which changed the vortex-shedding pattern

Author	*Re*	Method	Azimuth
Amitay *et al*. (1997)	4000 75 500	Smoke visualization, pressure measurement	0–180°
Amitay, Smith & Glezer (1998)	75 500	Hot-wire	60°
Crook, Sadri & Wood (1999)	550 000	Surface flow visualization	93.5°
Béra *et al*. (2000)	133 000	Pressure measurement, PIV	110°
Tensi *et al*. (2002)	100 000	Pressure measurement, wall visualization, PIV	60, 112.5 and 180°
Fujisawa & Takeda (2003)	9000	Pressure and force measurement, PIV	60–120°
Fujisawa, Takeda & Ike (2004)	9000	Pressure and force measurement, PIV	90°
Wang, Feng & Xu (2007)	1000	Flow visualization	0°
Feng *et al.* (2008)	1000	Flow visualization	180°

TABLE 1. Summary of circular cylinder flow control by a synthetic jet.

remarkably. Meanwhile, the instantaneous flow field did not show periodic vortex shedding when the slot was larger than the critical width. Mittal (2003), Hwang, Yang & Sun (2003), Akilli, Sahin & Tumen (2005) and Akilli *et al.* (2008) indicated that a splitter plate attached to the rear stagnation point or inside the wake region could suppress the vortex shedding partly or completely, and even reduce the drag force and lift fluctuations.

To sum up, the rear stagnation point perturbations based on the synthetic jet is a novel control arrangement, which is lacking deep investigation. This work particularly investigates the influence of the synthetic jet positioned at the mean rear stagnation point on the wake-vortex structures around the circular cylinder. The effects of the large-scale coherent structures on the velocity fluctuations and Reynolds stresses of the global flow field are also analysed by means of a particle-image-velocimetry (PIV) measurement. In the following, § 2 introduces the experimental set-up and § 3 presents data-processing methods. Basic information of the synthetic jet is then introduced in § 4. Dynamics of the vortex structures, including vortex-synchronization phenomena, variations of the vortex-shedding mode and vortex evolution, are given attention in § 5. The influence of the coherent structures on the velocity fluctuations and Reynolds stresses is discussed in §6. Flow topology is examined in § 7. Finally, the conclusion and discussion are given in § 8.

2. Experimental set-up

2.1. *Experimental model*

The experiment was conducted in a low-speed recirculation water channel, which had a Plexiglas test section of 600 mm × 600 mm and a length of 4800 mm. The free-stream velocity could be continuously changed in the range of lower than 200 mm s^{-1} and the streamwise turbulence intensity was no more than 0.8 %. The experimental model was a hollow circular cylinder with outer diameter $D = 30$ mm, inner diameter $d = 22$ mm and length 500 mm, as shown in figure 1. The coordinate system was defined such that the origin was located at the centre of the cylinder, with x-axis and y-axis representing the streamwise and transverse directions, respectively. The circular cylinder was horizontally mounted across the test section, with a vertical distance of about $8.33D$ to both the bottom and top free surface of the test section. This gave a blockage ratio of 6 %. In order to maintain the two-dimensionality of the flow field,

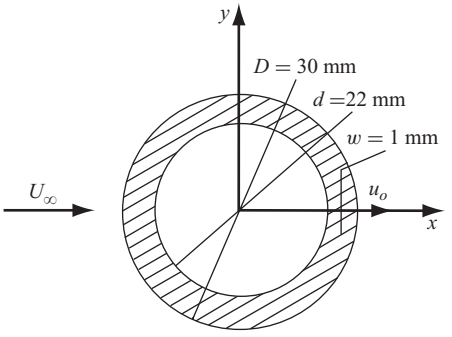

FIGURE 1. Schematic of the experimental circular cylinder.

the inside end of the circular cylinder was attached to one end plate with height $20D$, length $50D$ and thickness 10 mm. The end plate was parallel to the inside wall of the test section and had a distance of $3D$ from it to avoid the oncoming boundary layer (Szepessy & Bearman 1992). It had a 4:1 elliptical leading edge to avoid flow separation, with $10D$ from the cylinder centre. However, no end plate was used for the outside end of the circular cylinder to avoid any additional light refraction when using the charge-coupled device (CCD) camera. This end was secured on the outside wall of the water channel directly. Since the flow was kept laminar, the thickness of the boundary layer developing on the outside wall at the location of the circular cylinder was no more than $0.5D$. Thus, it would not have a strong influence on the test section, which was the very-near-wake region and about $8.33D$ from both ends of the circular cylinder, according to Konstantinidis & Balabani (2007).

A slot with width $w = 1$ mm and length $l = 50$ mm was disposed on the external surface in the mid-span region of the experimental circular cylinder and parallel to its axis. The length of the slot was selected as $1.67D$ since it could ensure a well-developed two-dimensional synthetic-jet flow, which could not be guaranteed with a longer slot. Therefore, its effect on the wake vortex was also two-dimensional, though the ends of the slot jet did have some three-dimensional effect on the wake vortex. However, as mentioned above, this study focused on the very-near-wake region of the cylinder in the mid-span of the slot. Thus, the three-dimensional effect introduced by the ends of the synthetic-jet flow would also have no crucial influence. This has been confirmed in the previous work by Feng *et al.* (2008), which indicated that the influenced wake flow by a $1.67D$ synthetic jet was kept two-dimensional very well in the near wake.

An 'L'-shaped hollow cylinder with outer diameter 30 mm and inner diameter 24 mm was vertically connected to the experimental cylinder. There was a piston with diameter $D_p = 24$ mm inside the vertical cylinder cavity and it was connected to a servo electromotor with a centre-setting crank mechanism (formed by an eccentric disk and a connecting rod). The servo electromotor could perform a cycle motion. Meanwhile, the piston had a reciprocating motion. Thus, the fluid inside the cavity would be injected and sucked from the slot, and then the synthetic-jet vortex pair was generated. The frequency of the vortex-pair formation was equal to that of the servo electromotor motion so that we could alter the frequency of the synthetic jet by adjusting the rotation speed of the servo electromotor.

2.2. *Experimental parameters*

During the experiment, the free-stream velocity was fixed at $U_\infty = 41.8\,\mathrm{mm\,s^{-1}}$, corresponding to the circular cylinder Reynolds number $Re = 950$. For this Reynolds

number, the flow around the circular cylinder is in the subcritical state (Zdravkovich 1997). The natural Kármán-vortex-shedding frequency is $f_o = 0.30$ Hz, corresponding to the Strouhal number $St = 0.215$, which will be further validated in figure 5(*a*). The exit slot of the synthetic jet was fixed at the mean rear stagnation point of the circular cylinder, which was $x/D = 0.5$, $y/D = 0$, as shown in figure 1.

The synthetic-jet exit velocity could be estimated based on mass conservation given by

$$u_o = \frac{\pi^2 D_p^2}{2lw} A f_e \sin(2\pi f_e t), \tag{2.1}$$

where A is the amplitude of the eccentric disk, f_e is the excitation frequency and t is the excitation time. In order to analyse the flow structures of the synthetic jet in a quiescent environment, Smith & Glezer (1998) proposed a slug model including two primary parameters. One was the dimensionless stroke length L. An elementary representation of this parameter was the displacement of the jet flux having the exit velocity during the blowing cycle, normalized by the slot width, which was given by

$$L = \frac{\pi D_p^2}{2lw^2} A. \tag{2.2}$$

Another was the Reynolds number $Re_{\overline{U_o}}$ based on the time-averaged blowing velocity over one entire cycle and was given by

$$Re_{\overline{U_o}} = \frac{\pi D_p^2}{2\nu l} A f_e, \tag{2.3}$$

where ν is the fluid kinematic viscosity. Many other investigations after Smith & Glezer (1998) all proved that the synthetic jet was distinguished by the slug model (see the review by Zhang *et al.* 2008). According to Shuster & Smith (2007), the distance of vortex pair from the exit increased with the stroke length L, while the vortex strength increased with the Reynolds number $Re_{\overline{U_o}}$, but the location of the vortex centre was not affected by the Reynolds number.

The variable parameters for the synthetic-jet actuator were the amplitude of the eccentric disk A and the excitation frequency f_e. As given in (2.2) and (2.3), L only depends on A, while $Re_{\overline{U_o}}$ is determined by both A and f_e. The excitation amplitude A was set at 5.5 mm, and the excitation frequency f_e was selected at 0.15, 0.25, 0.50, 0.75, 1.00 and 1.50 Hz, corresponding to the dimensionless frequency $f_e/f_o =$ 0.50, 0.83, 1.67, 2.50, 3.33 and 5.00, respectively. The corresponding Reynolds numbers were $Re_{\overline{U_o}} = 11$, 19, 38, 57, 76 and 114, respectively, while the dimensionless stroke length L was 99.5 for all the controlled cases. This is aimed at changing the strength of the synthetic-jet vortex pair, which we deduce should be the crucial effect that determines the interaction between the synthetic jet and the wake vortex rather than the excitation frequency.

2.3. *PIV measurement*

The circular cylinder flow field was measured by the PIV technique. The flow field was illuminated by a light sheet from an Nd:YAG (neodymium-doped yttrium aluminium garnet) successive laser, which emitted 532 nm wavelength light. The tracer particles were hollow glass beads with average diameter 5 μm and density 1.05 g mm^{-3}. The field of view was captured by a high-speed CCD camera. The CCD camera used a Navitar TV lens with the focal length of 50 mm, focal ratio (f-number) of 0.95 and depth of field of 6.3 mm. It had a spatial resolution of 640 pixels × 480 pixels with 8 bits in grey scale. Thus, the size of the measurement area could be approximately

up to $3D \times 2D$ due to the resolution of the CCD. The sampling frequency of the high-speed CCD was selected at 100 Hz with the exposure time of 5 ms. A total of 10 000 frames were recorded continuously in one case.

Since the exit of the synthetic jet was fixed, once the experimental model had been installed, it was no longer necessary to touch it in the water. The only thing that was changed was the rotation speed of the servo electromotor, by changing the excitation frequency. Since the piston was isolated from the water from the 'L'-shaped hollow cylinder, it did not introduce any disturbances into the free stream. Moreover, the water channel had a good flow quality so that during the experiment there were no significant surface disturbances that had any influence on the running of the laser and the CCD camera.

A grey-level-difference algorithm was applied for the cross-correlation calculation between two successive images. The sizes of the interrogation window and search window were set to 16 pixels × 16 pixels and 8 pixels × 8 pixels, respectively. Gaussian peak fit was applied to enhance the resolution of cross-correlation peak identification to a subpixel level. Multi-grid iteration with window deformation was also used to improve the trace accuracy of the interrogation window. The uncertainty of the particle displacement was less than 0.1 pixel at different image shift position with the image magnification of 0.14 mm pixel^{-1}. Since the sampling frequency was 100 Hz, the uncertainty velocity would be 1.98 mm s^{-1}, which yielded an uncertainty of 4.74 % relative to the free-stream velocity. The spanwise vorticity was calculated by the difference of the velocity field, thus its uncertainty was about 1.65 s^{-1}, which was 1.18 normalized by the cylinder diameter and free-stream velocity, based on the error-analysis theory (Raffel *et al.* 2007; Bendat & Piersol 2010).

3. Data processing

3.1. *Phase averaging*

The synthetic jet is a periodic event and the time durations of different cycles are almost the same. Therefore, it is easy to determine the phase of any time as long as the start phase has been chosen. However, the Kármán-vortex shedding is a quasi-periodic event. Thus, the phase relationship should not be determined by simple time adding. Some physical quantities in the flow field around the circular cylinder are usually used as a reference for phase determination. For instance, the pressure signal near the separation point was measured for the required reference phase by Cantwell & Coles (1983). Zhou, Zhang & Yiu (2002) and Zhou & Yiu (2006) extracted the phase information from the spanwise velocity at the irrotational region outside the wake and successfully separated the coherent and incoherent flow fields. Kim *et al.* (2006) adopted the streamwise velocity at $x/D = 1.5$, $y/D = 0.5$ as a reference.

In this paper, the phase-determination technique is combined with that of Zhou *et al.* (2002), Zhou & Yiu (2006) and Kim *et al.* (2006). The streamwise velocity $u(t)$ at a certain position of the flow field is filtered first to eliminate background disturbances, and then a much smoother filtered signal $u_f(t)$ is obtained, as shown in figure 2. A moving-average technique, which replaces any point of data by its surrounding five points has been used. Thus, the filtered signal has nearly no time delay compared with the original signal. Two typical phases could be determined from $u_f(t)$, which are phases A (0 or 2π) and B (π). Phase A (0 or 2π) is designated to each maximum time t_A in the amplitude of the signal $u_f(t)$ and phase B (π) is designated to each minimum time t_B. The phase interval between phases A and B is π,

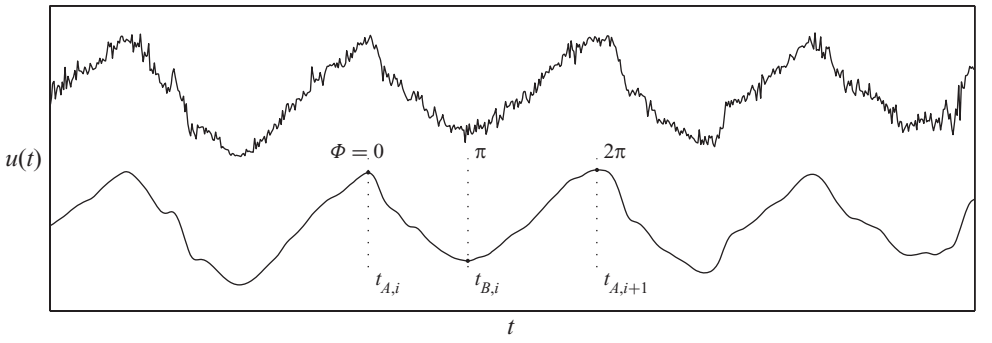

FIGURE 2. Signal filtering and phase determining.

the time interval $t_{AB,i}$ is

$$t_{AB,i} = t_{B,i} - t_{A,i} \tag{3.1}$$

and the time interval $t_{BA,i}$ is

$$t_{BA,i} = t_{A,i+1} - t_{B,i}. \tag{3.2}$$

Then any other phases could be determined based on the decided times t_A and t_B as follows:

$$\Phi = \pi \frac{t - t_{A,i}}{t_{B,i} - t_{A,i}}, \quad t_{A,i} \leqslant t < t_{B,i}, \tag{3.3}$$

$$\Phi = \pi \frac{t - t_{B,i}}{t_{A,i+1} - t_{B,i}} + \pi, \quad t_{B,i} \leqslant t < t_{A,i+1}. \tag{3.4}$$

For the natural case, the reference signal $u(t)$ is selected at $x/D = 2.5$, $y/D = 0.6$. The duration between phases A and B is equally divided into 36 phases. Thus, the phase interval is $\pi/36$ and time interval is 0.046 s. The reference signal of the controlled cases is selected near the rear stagnation point at $x/D = 0.6$, $y/D = 0$. Phase 0 is defined as the start of the blowing cycle of the synthetic jet and phase π is the start of the suction cycle. Because the cycle duration is kept constant, every frame could be recognized as part of the phase evolution. The duration between phases A and B is divided into $50/f_e$ phases according to different excitation frequencies. Therefore, the phase interval is $\pi f_e/50$ and the time interval is 0.01 s.

Phase averaging could be carried out by adding the instantaneous quantity after the phase of any time has been determined as follows:

$$\langle s_i \rangle = \frac{1}{N_i} \sum_{n=1}^{N_i} s_{i,n}, \tag{3.5}$$

where s represents arbitrary physical quantities in the flow fields, including velocity, velocity fluctuation, spanwise vorticity and Reynolds stress, N_i is the number of samples at phase i and '$\langle\ \rangle$' represents phase averaging of physical quantities. Similarly, time averaging of arbitrary physical quantities is given by

$$\bar{s} = \frac{1}{N} \sum_{n=1}^{N} s_n, \tag{3.6}$$

where N is the number of total samples and '$\bar{}$' means time averaging of physical quantities.

3.2. *Velocity decomposition*

To investigate different contributions of the large- and small-scale vortex structures, Cantwell & Coles (1983), Balachandar, Mittal & Najjar (1997), Govardhan & Williamson (2001), Sung & Yoo (2003), Konstantinidis *et al.* (2005*b*), Kim *et al.* (2006) and Konstantinidis & Balabani (2008) all applied the velocity triple-decomposition method proposed by Reynolds & Hussain (1972). The physical quantity s in the flow field is divided into a global mean component $\bar{s}$ and a total fluctuation component s':

$$s = \bar{s} + s'. \tag{3.7}$$

The total fluctuation component s' can be further decomposed into a periodic mean component $\tilde{s}$ and a random component $\hat{s}$:

$$s = \bar{s} + \tilde{s} + \hat{s}. \tag{3.8}$$

The periodic mean component $\tilde{s}$ is defined as the difference between the phase-averaged component and the time-averaged component:

$$\tilde{s} = \langle s \rangle - \bar{s}. \tag{3.9}$$

The periodic mean component $\tilde{s}$ reflects contributions of the large-scale organized coherent structures, while the random component $\hat{s}$ reflects contributions of the small-scale turbulent structures (Reynolds & Hussain 1972; Cantwell & Coles 1983; Kim *et al.* 2006). The conventional total Reynolds stresses are based on the total fluctuation component s'. It can be further divided into the coherent Reynolds stresses and incoherent Reynolds stresses, which are calculated from the periodic mean component $\tilde{s}$ and the random component $\hat{s}$, respectively. Similarly, the coherent Reynolds stresses are produced by the large-scale organized coherent structures, while the incoherent Reynolds stresses are produced by the small-scale turbulent structures. Phase-averaged and time-averaged components have the following relationships:

$$\langle s'q' \rangle = \langle \tilde{s}\tilde{q} \rangle + \langle \hat{s}\hat{q} \rangle, \tag{3.10}$$

$$\overline{s'q'} = \overline{\tilde{s}\tilde{q}} + \overline{\hat{s}\hat{q}}, \tag{3.11}$$

where s and q represent arbitrary combinations of the streamwise velocity u and the transverse velocity v.

3.3. *Vortex-centre detection*

In order to analyse the evolution of vortex structures, the location of the vortex centre is determined. There are usually two definitions of the vortex centre: one is the peak position of the vorticity field and the other is the centroid of the vorticity (Cantwell & Coles 1983; Sung & Yoo 2003; Konstantinidis *et al.* 2005*a*; Huang, Zhou & Zhou 2006; Kim *et al.* 2006). The former is easy to realize but may result in high uncertainty, especially when the resolution of the vorticity field is too low or the coherent structure is not well preserved. Thus, the vortex centroid proposed by Cantwell & Coles (1983) is applied in this research. It can be obtained by the integration of the vorticity field above a given threshold

$$\omega_z = \frac{\partial V}{\partial x} - \frac{\partial U}{\partial y}, \tag{3.12}$$

$$\Gamma = \int_S \omega_z \, \mathrm{d}S, \tag{3.13}$$

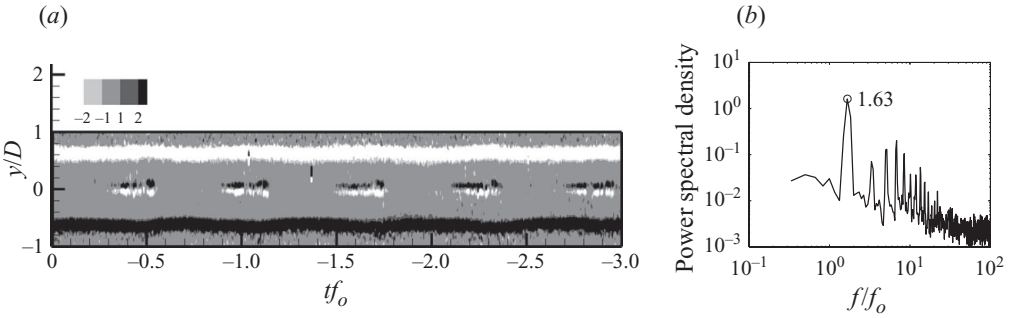

FIGURE 3. (*a*) Evolution of the instantaneous spanwise vorticity $\omega_z D/U_\infty$ near the exit at $x/D=0.7,\ -1\leqslant y/D\leqslant 1$, and (*b*) power spectral density of $\omega_z D/U_\infty$ at $x/D=0.7,\ y/D=0.06$, for $f_e/f_o=1.67$.

$$x_c=\frac{1}{\Gamma}\int_S x\omega_z\,\mathrm{d}S, \tag{3.14}$$

$$y_c=\frac{1}{\Gamma}\int_S y\omega_z\,\mathrm{d}S, \tag{3.15}$$

where ω_z is the spanwise vorticity, Γ is the circulation, S is the integration area and x_c and y_c are the coordinates of the vortex centroid. The integration is performed only for values of $\omega_z/\omega_{zp}\geqslant 0.5$, where ω_{zp} is the local peak, in order to avoid relatively noisy data, according to Sung & Yoo (2003) and Kim *et al.* (2006). However, the integration area is hard to determine when the wake vortex is not formed completely and still connects to the separation shear layer. Ultimately, the region of $x/D\geqslant 1.8$ is selected for the integration of the wake vortex, while the integration region is $x/D\geqslant 0.5$ for the synthetic-jet vortex.

4. Basic information on the synthetic jet

The essential characteristic of the synthetic jet is to induce vortex pairs near the exit periodically, which then convect downstream and, thus, bring periodic perturbations into the external flow (Smith & Glezer 1998; Shuster & Smith 2007). This characteristic will be illustrated in the following by the controlled case $f_e/f_o=1.67$.

Figure 3 presents the evolution of the instantaneous spanwise vorticity $\omega_z D/U_\infty$ near the exit at $x/D=0.7,\ -1\leqslant y/D\leqslant 1$, and the power spectral density of $\omega_z D/U_\infty$ at $x/D=0.7,\ y/D=0.06$ for the case $f_e/f_o=1.67$. The time coordinate is from big to small and the flow direction is from left to right, which suggests that the spanwise vorticity in figure 3 is passing through the observation point from right to left. The dimensionless time $tf_o=0$ is defined as the start of the blowing cycle of the synthetic jet. Figure 3(*a*) shows that there are synthetic-jet vortex pairs near the x-axis, which are passing through the observation point periodically. There also exist strong shear layers behind both sides of the circular cylinder near $y/D=\pm 0.6$ due to flow separation. Power-spectral-density analysis is adopted to detect the dominant frequency. Following Jukes *et al.* (2006), the spectra multiplied by the variance of original signal are normalized by the integral spectra over the entire dimensionless frequency range, as shown in figure 3(*b*) (the same as in figures 4*b* and 5 in the following). There exists an absolute uncertainty of ± 0.024 Hz for the power-spectral-density result, corresponding to the dimensionless uncertainty of ± 0.08 when normalized by the natural shedding frequency f_o. It shows that the dominant frequency f/f_o of the synthetic jet is 1.63,

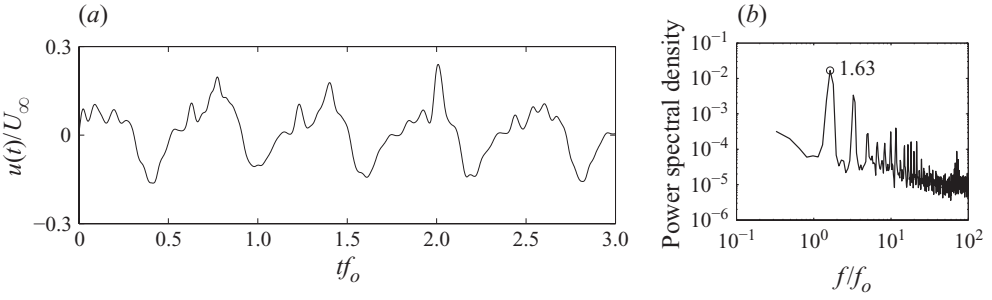

FIGURE 4. (*a*) Evolution of the instantaneous streamwise velocity $u(t)/U_\infty$, and (*b*) power spectral density of $u(t)/U_\infty$ near the exit at $x/D = 0.6,\ y/D = 0$, for $f_e/f_o = 1.67$.

which is in the range of uncertainty compared with the actual excitation frequency f_e/f_o of 1.67. Note that the intense fluctuation at high frequencies is due to noises in the PIV data. The synthetic-jet vortex pairs are also induced near the exit periodically at other excitation frequencies, which is the essential characteristic of the synthetic jet. However, this characteristic at other excitation frequencies will not be presented here due to its similarity to that of $f_e/f_o = 1.67$.

Figure 4 presents the time history of the streamwise velocity $u(t)/U_\infty$ near the exit at $x/D = 0.6,\ y/D = 0$ and the corresponding power spectral density. Figure 4(*a*) shows that the exit velocity is positive at the blowing cycle and negative at the suction cycle, and exhibits a sinusoidal characteristic. The power spectral density illustrates the dominant peak $f/f_o = 1.63$ and its several harmonics (see figure 4*b*). The synthetic-jet exit velocity also exhibits obvious periodic characteristic at other excitation frequencies, while it is enhanced with the increase in the excitation frequency.

5. Dynamics of vortex structures

5.1. *Vortex-synchronization phenomenon*

The vortex-synchronization phenomenon is usually verified by the power-spectral-density analysis of the physical quantities in flow field, such as velocity, velocity fluctuation and vorticity. The dominant frequency obtained by these physical quantities is usually the same. Therefore, the dimensionless spanwise vorticity $\omega_z D/U_\infty$ at several representative streamwise positions in the near-wake region $0.5 \leqslant x/D \leqslant 3,\ y/D = 0.6$ is applied for the power-spectral-density analysis. The spectra for $x/D \geqslant 2.5$ validate that the Kármán-vortex-shedding frequency is $f_o = 0.30$ Hz for the natural case, corresponding to the Strouhal number $St = 0.215$ (see figure 5*a*). For $f_e/f_o = 0.83$ (see figure 5*b*), the spectra in the region $x/D \leqslant 2.25$ show a dominant dimensionless frequency of 0.82, indicating that the flow fields in this region are influenced by the synthetic jet. However, the spectra for $x/D \geqslant 2.75$ exhibit the natural Kármán-vortex-shedding frequency again. The exit velocity further increases for higher excitation frequencies, resulting in the enlargement of the flow region dominated by the synthetic jet. Figures 5(*c*)–5(*f*) demonstrate the existence of the dominant frequencies $f/f_o = 1.63$, 2.44, 3.26 and 5.05 in the region $0.5 \leqslant x/D \leqslant 3$, which are 0.04, 0.06 and 0.07 lower and 0.05 higher than the theoretical values $f_e/f_o = 1.67$, 2.50, 3.33 and 5.00, respectively. As mentioned above, they are in the range of spectral-analysis uncertainty. Consequently, figures 5(*c*)–5(*f*) suggest that vortex synchronization occurs in the range $1.67 \leqslant f_e/f_o \leqslant 5.00$, which will be further validated in the following by the evolution of the spanwise vorticity.

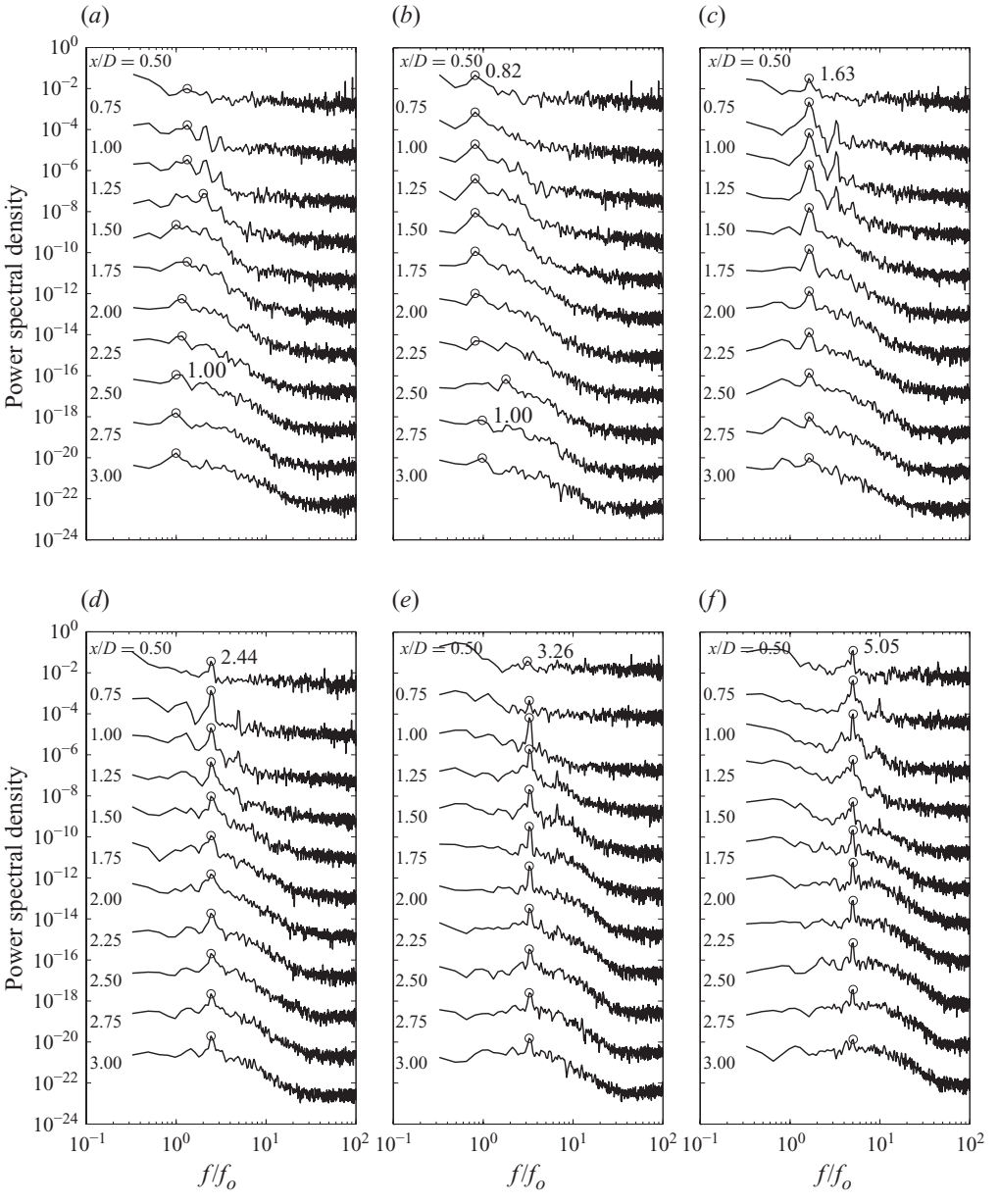

FIGURE 5. Power spectral density of the spanwise vorticity $\omega_z D/U_\infty$ in the near wake at $0.5 \leqslant x/D \leqslant 3$, $y/D = 0.6$. From $x/D = 0.75$ to 3, each power spectral density has been shifted downwards by 100 compared with the former one. (*a*) Natural; (*b*) $f_e/f_o = 0.83$; (*c*) 1.67; (*d*) 2.50; (*e*) 3.33; (*f*) 5.00.

5.2. *Evolution of vortex structures*

Figure 6 presents the phase-averaged spanwise vorticity $\langle\omega_z\rangle D/U_\infty$ of the global field at four phases of 0, 0.5π, π and 1.5π for both the natural- and vortex-synchronization cases. Figures 6(*a*)–6(*d*) show that the upper wake vortex starts to form and shed downstream, while the lower wake vortex exhibits the opposite progress. This is exactly the typical antisymmetric shedding mode. The controlled cases are presented

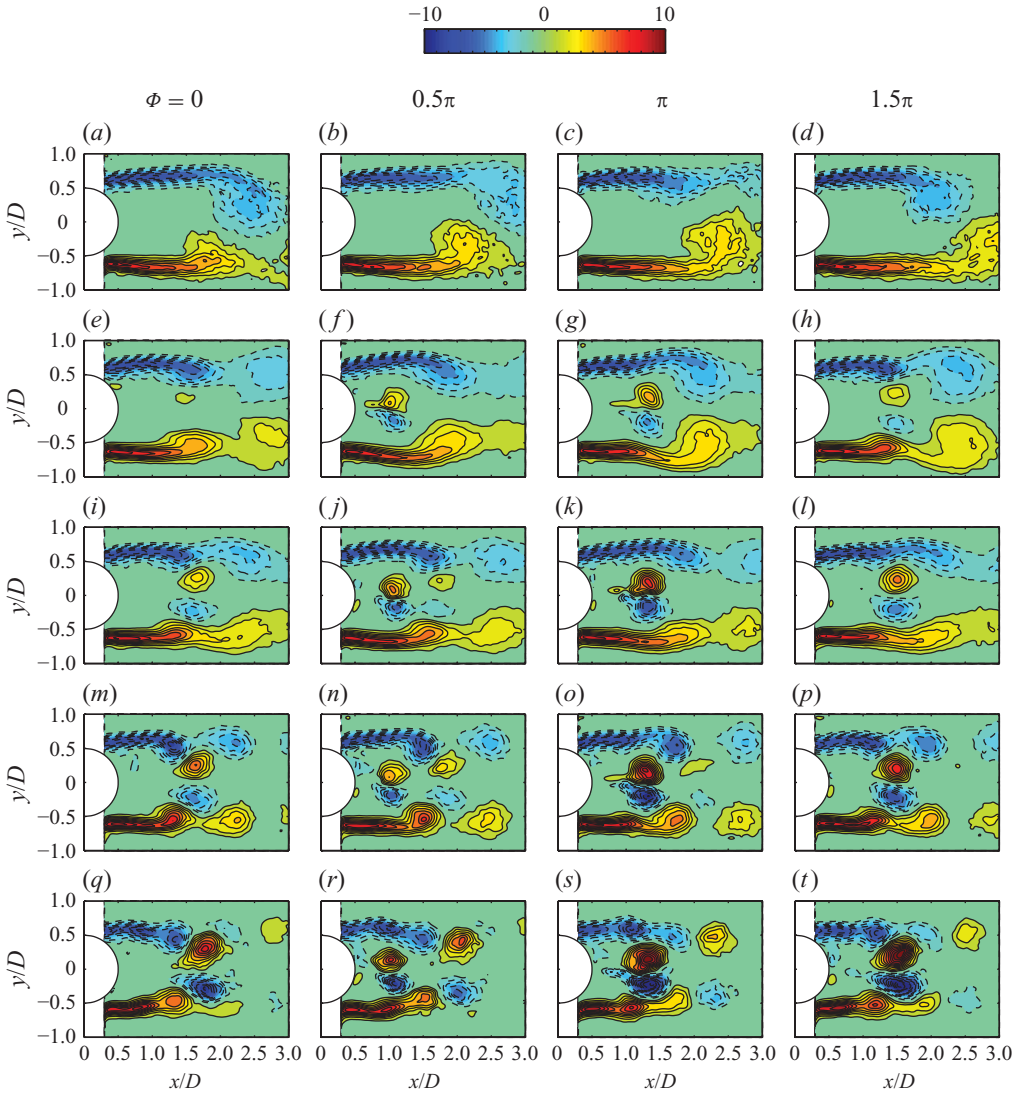

FIGURE 6. Phase-averaged spanwise vorticity $\langle\omega_z\rangle\, D/U_\infty$ of the global field at four phases of 0, 0.5π, π and 1.5π for the natural- and vortex-synchronization cases. (*a–d*) Natural; (*e–h*) $f_e/f_o = 1.67$; (*i–l*) 2.50; (*m–p*) 3.33; (*q–t*) 5.00. Contour levels: ± 1.

in figures 6(*e*)–6(*t*). It is shown that the streamwise position of the synthetic-jet vortices is nearly the same at an identical phase for different excitation frequencies, while the vorticity strength is much greater at a higher excitation frequency. The synthetic-jet vortices interact with the vorticity shear layers behind both sides of the circular cylinder as they are convected downstream, resulting in the concentration of vorticities near the tails of the shear layers. The concentrated vorticities will then separate from the shear layer and roll up into vortex structures. Afterwards, the new induced wake vortices shed downstream under the free stream and the crowding-out effect of the synthetic-jet vortex pairs. The strength of the synthetic-jet vortex decreases gradually and the distance to the new induced wake vortex increases. Finally, the synthetic-jet vortices disappear completely and there only exist wake vortices shedding

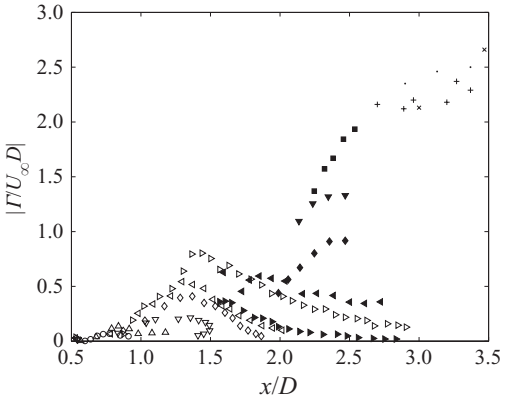

FIGURE 7. Streamwise evolution of the circulation $|\Gamma/U_\infty D|$ for the synthetic-jet vortex and the wake vortex. ■, Natural; ○, $f_e/f_o = 0.50$; △, 0.83; ▽, ▼, 1.67; ◇, ◆, 2.50; ◁, ◀, 3.33; ▷, ▶, 5.00; •, Cantwell & Coles (1983); +, Konstantinidis *et al.* (2005*b*); ×, Huang *et al.* (2006). The empty and filled symbols represent the synthetic-jet vortex and wake vortex, respectively.

downstream. Note that the synthetic-jet vortex pair and the new induced wake vortex all shed downstream with an almost-symmetric shedding mode, and they have a one-to-one correspondence with each other with an approximate phase difference of π. The induction effect of the synthetic jet upon the wake vortex is more significant as the excitation frequency increases. Thus, the induced wake vortices are more obvious at higher excitation frequencies. They separate from the shear layer and completely form at a much more upstream position, suggesting that the formation length of the new induced wake vortex is shortened. It is worth noticing that for $f_e/f_o = 5.00$ (see figures 6*q*–6*t*), the new wake vortices are attenuated more quickly than other controlled cases due to the strong induction effect of the synthetic-jet vortices.

The evolution of the circulation $|\Gamma/U_\infty D|$ for both the synthetic-jet vortex and wake vortex is presented in figure 7. The empty and filled symbols represent the synthetic-jet vortex and wake vortex, respectively. Only the vortices developing in the range $y/D \geqslant 0$ are analysed due to the symmetry of the flow field, corresponding to the positive synthetic-jet vortex and the negative wake vortex. The circulation of the synthetic-jet vortex at different frequencies reaches the maximum and then decreases gradually, and the circulation is much greater at a higher excitation frequency. The circulation of the new induced wake vortex is lower than that of the Kármán vortex, and it is much lower at a higher excitation frequency. Figure 7 also presents the statistical results of the Kármán vortex from Cantwell & Coles (1983), Konstantinidis *et al.* (2005*b*) and Huang *et al.* (2006). The present wake-vortex circulation is calculated in the range $x/D \leqslant 3$, where the Kármán vortex has not yet fully formed, and the integration area is also smaller than that of Cantwell & Coles (1983) and Huang *et al.* (2006). Consequently, the vortex circulation in this paper is smaller than theirs. However, the present trend is consistent with previous studies.

Figure 8 presents the streamwise and transverse trajectories for both the synthetic-jet vortex and the wake vortex. The symbols are the same as given in figure 7. The cubic-curve-fitting results of the trajectories are also shown. The dashed and solid lines denote the synthetic-jet vortex and wake vortex, respectively. As shown in figure 8, the streamwise and transverse trajectories of the synthetic-jet vortex are almost coincident within $t/T \leqslant 0.8$ for $1.67 \leqslant f_e/f_o \leqslant 5.00$. After $t/T \geqslant 0.8$, the

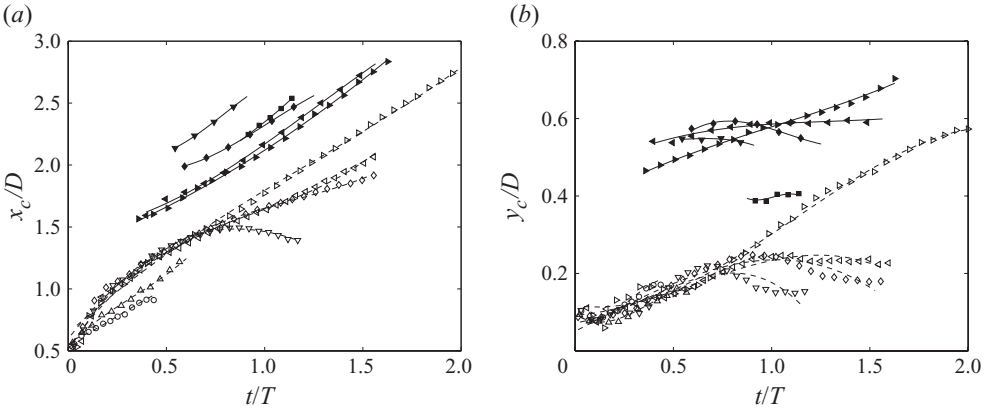

FIGURE 8. Trajectories of the synthetic-jet vortex and the wake vortex: (*a*) streamwise trajectories; (*b*) transverse trajectories. Symbols are same as given in figure 7. The dashed and solid lines denote the synthetic-jet vortex and wake vortex, respectively.

synthetic-jet vortex can reach up to a further streamwise and transverse downstream position at a higher excitation frequency. The streamwise and transverse trajectories have a higher slope as the excitation frequency increases, indicating that both the streamwise and transverse convection velocities of the synthetic-jet vortex increase with the excitation frequency. The streamwise trajectories of the induced wake vortex are affected by the synthetic-jet vortex, which demonstrates that they are much closer upstream at a higher frequency (see figure 8*a*). However, as can be deduced from the slope of the streamwise trajectory, the streamwise convection velocities of the induced wake vortex do not vary very much at different excitation frequencies, compared with the natural Kármán vortex. The transverse locations of the induced wake vortex are approximately $0.2D$ higher than that of the natural case (see figure 8*b*). They change slightly with time for the natural and $1.67 \leqslant f_e/f_o \leqslant 3.33$ cases, whereas, for $f_e/f_o = 5.00$, it has an obvious transverse moving process due to the strong crowding-out effect of the synthetic-jet vortex, which moves towards both sides while shedding downstream.

6. Influence of coherent structures on velocity fluctuations and Reynolds stresses

Cantwell & Coles (1983), Balachandar *et al.* (1997) and Kim *et al.* (2006) all concluded that large-scale organized coherent structures determined the distributions of the velocity fluctuations and Reynolds stresses in the flow field, which satisfies the four-quadrant-type distribution rule defined by Balachandar *et al.* (1997). The influence of the synthetic-jet vortex and new induced wake vortex with a symmetric shedding mode on the distributions of the velocity fluctuations and Reynolds shear stresses will be studied and compared with that of the natural Kármán vortex. It will be illustrated by the comparison between the natural and $f_e/f_o = 3.33$ cases in the following.

6.1. *Phase-averaged results*

Figure 9 shows phase-averaged periodic mean streamwise fluctuation $\langle \tilde{u} \rangle / U_\infty$ for both the natural and $f_e/f_o = 3.33$ cases. In order to reveal the information of the vortex structures on the distributions of the velocity fluctuations and Reynolds stress, the

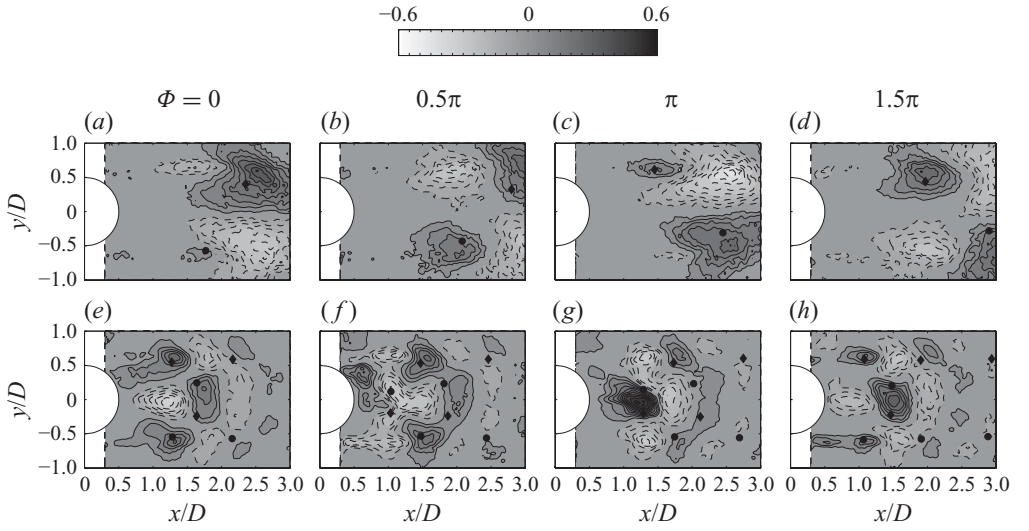

FIGURE 9. Phase-averaged periodic mean streamwise fluctuation $\langle\tilde{u}\rangle/U_\infty$ at four phases of 0, 0.5π, π and 1.5π for the natural (*a–d*) and $f_e/f_o = 3.33$ (*e–h*) cases. The black solid circles and diamonds denote positions of the positive and negative vortex centres, respectively. Contour levels: ±0.05.

positions of the positive and negative vortex centres are also denoted by the black solid circles and diamonds, respectively (the same as figures 10 and 11 in the following). Figures 9(*a*)–9(*d*) indicate that $\langle\tilde{u}\rangle$ is congregated beyond $x/D = 1.5$ at different phases. It is also antisymmetric about the x-axis due to the antisymmetric shedding of the Kármán vortex. For $f_e/f_o = 3.33$ (see figures 9*e*–9*h*), the periodic mean streamwise fluctuation is symmetric about the x-axis because of the symmetric shedding mode of both the synthetic-jet vortex and wake vortex, whereas the distributions of $\langle\tilde{u}\rangle$ become much more complicated since there exist several vortex pairs in the flow field at the same phase.

Figure 10 presents variations of the phase-averaged periodic mean transverse fluctuation $\langle\tilde{v}\rangle/U_\infty$. Figures 10(*a*)–10(*d*) indicate that $\langle\tilde{v}\rangle$ is symmetric about the x-axis and becomes congregated beyond $x/D = 1.5$ at different phases for the natural case. For $f_e/f_o = 3.33$ (see figures 10*e*–10*h*), $\langle\tilde{v}\rangle$ is antisymmetric about the x-axis and congregates around the vortex centres but with a smaller scale. The distributions of $\langle\tilde{v}\rangle$ for both cases are all antisymmetric about the vortex centre in the streamwise direction. The transverse-velocity fluctuations on the left and right of the clockwise vortex are positive and negative, respectively, while the anticlockwise vortex produces the transverse fluctuations of opposite sign. This is in good agreement with the quadrant distribution rule of Balachandar *et al.* (1997).

Figure 11 shows variations of the phase-averaged coherent Reynolds shear stress $\langle\tilde{u}\tilde{v}\rangle/U_\infty^2$. For the natural case (see figures 11*a*–11*d*), the distributions of $\langle\tilde{u}\tilde{v}\rangle$ at different phases are antisymmetric about the x-axis and the vortex centre in transverse and streamwise directions, respectively. They also congregate in the range $x/D > 1.5$. For $f_e/f_o = 3.33$ (see figures 11*e*–11*h*), the distributions of $\langle\tilde{u}\tilde{v}\rangle$ are also antisymmetric about the x-axis, but with a smaller congregation size. They are located close upstream surrounding the synthetic-jet vortices and the induced wake vortices, while their magnitudes are reduced when the induced wake vortices are shedding further downstream.

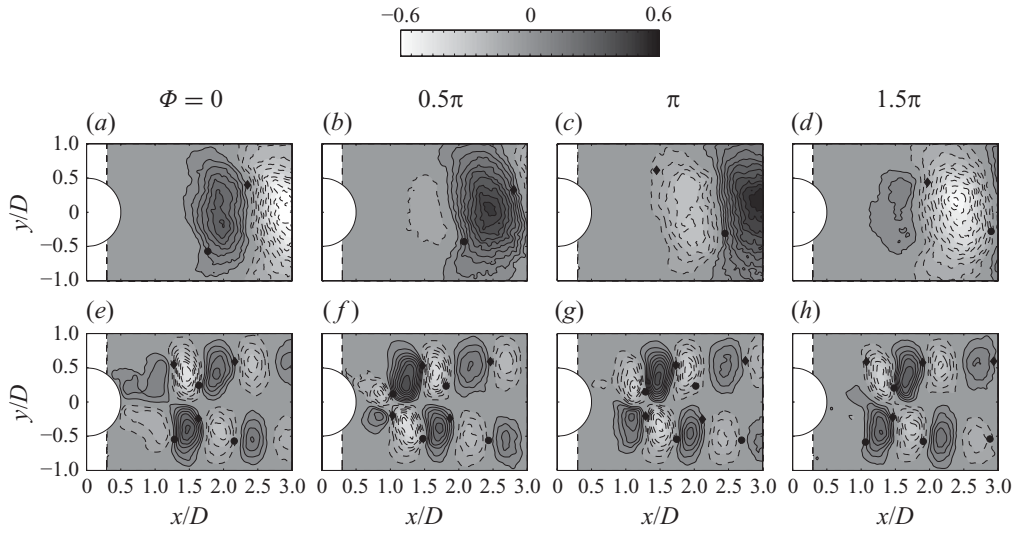

FIGURE 10. Phase-averaged periodic mean transverse fluctuation $\langle \tilde{v} \rangle / U_\infty$ at four phases of 0, 0.5π, π and 1.5π for the natural (*a–d*) and $f_e/f_o = 3.33$ (*e–h*) cases. The black solid circles and diamonds denote positions of the positive and negative vortex centres, respectively. Contour levels: ±0.05.

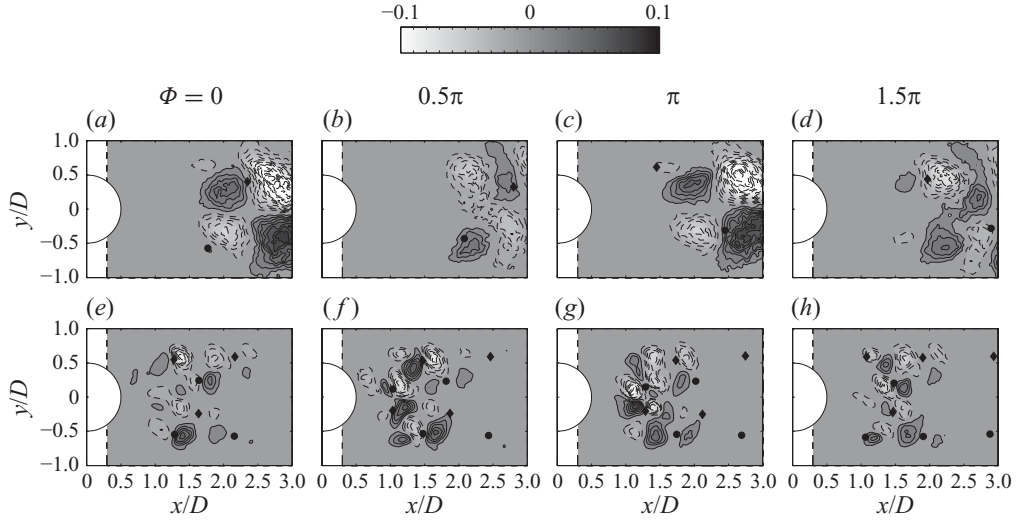

FIGURE 11. Phase-averaged coherent Reynolds shear stress $\langle \tilde{u}\tilde{v} \rangle / U_\infty^2$ at four phases of 0, 0.5π, π and 1.5π for the natural (*a–d*) and $f_e/f_o = 3.33$ (*e–h*) cases. The black solid circles and diamonds denote positions of the positive and negative vortex centres, respectively. Contour levels: ±0.01.

It is well known that the phase-averaged random fluctuations $\langle \hat{u} \rangle$ and $\langle \hat{v} \rangle$ are zero, while the phase-averaged coherent Reynolds normal stresses $\langle \tilde{u}\tilde{u} \rangle$ and $\langle \tilde{v}\tilde{v} \rangle$ are determined by the periodic mean fluctuations $\langle \tilde{u} \rangle$ and $\langle \tilde{v} \rangle$. Thus, it is indicated that the distributions of the velocity fluctuations and Reynolds stresses change essentially when the vortex shedding is converted into a symmetric mode from the original antisymmetric mode. However, the distributions are still dominated by the coherent

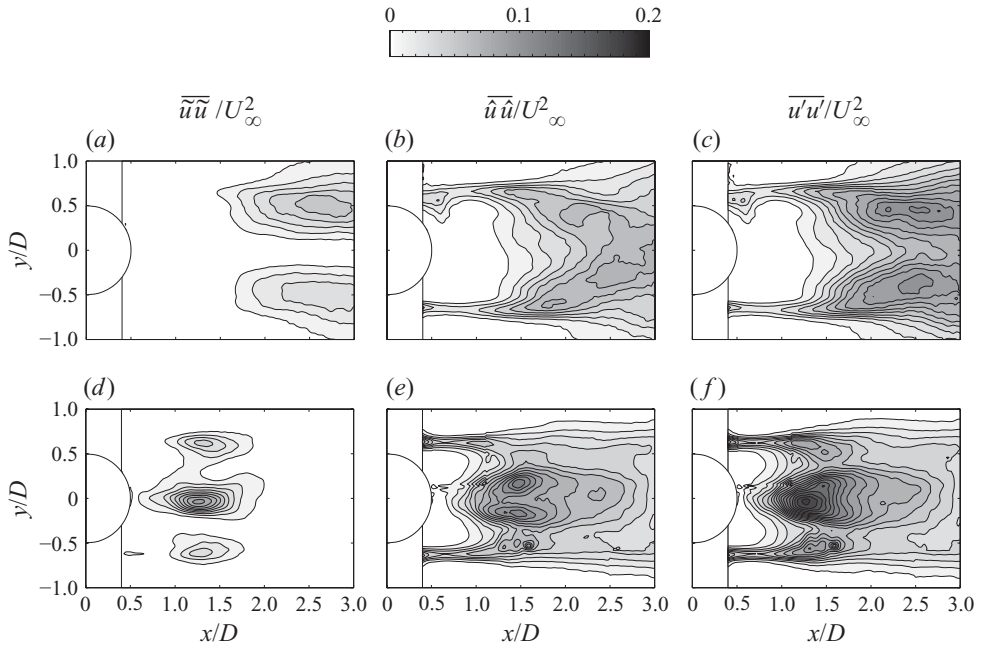

FIGURE 12. Time-averaged streamwise Reynolds normal stresses: $\overline{\tilde{u}\tilde{u}}/U_\infty^2$, $\overline{\hat{u}\hat{u}}/U_\infty^2$ and $\overline{u'u'}/U_\infty^2$ for the natural (*a–c*) and $f_e/f_o = 3.33$ (*d–f*) cases. Contour levels: 0.01.

vortex structures, which also accords with the four-quadrant-type distribution rule of Balachandar *et al.* (1997).

6.2. *Time-averaged results*

Figure 12 presents the time-averaged streamwise Reynolds normal stresses, including the coherent component $\overline{\tilde{u}\tilde{u}}$, the incoherent component $\overline{\hat{u}\hat{u}}$ and the total component $\overline{u'u'}$. Figures 12(*a*)–12(*c*) indicate that the Reynolds normal stresses all congregate beyond $x/D = 1.5$ for the natural case. The distributions of $\overline{\tilde{u}\tilde{u}}$ and $\overline{\hat{u}\hat{u}}$ show the peak-and-peak and single-peak patterns, respectively, which compose a peak-and-peak pattern of the total Reynolds normal stress $\overline{u'u'}$. For $f_e/f_o = 3.33$ (see figures 12*d*–12*f*), the distributions of $\overline{\tilde{u}\tilde{u}}$ and $\overline{u'u'}$ are triple-peak patterns with the middle peak much higher than both sides, while $\overline{\hat{u}\hat{u}}$ is a peak-and-peak pattern. The streamwise Reynolds normal stresses for the controlled case are higher than the natural case in the near wake, due to the streamwise stretching effect of the synthetic-jet vortex. Besides, their peaks move much more upstream compared with the natural case.

The time-averaged transverse Reynolds normal stresses are presented in figure 13. The distributions of $\overline{\tilde{v}\tilde{v}}$, $\overline{\hat{v}\hat{v}}$ and $\overline{v'v'}$ are all single-peak patterns with the peaks located near $x/D = 2.8$ for the natural case (see figures 13*a*–13*c*). They are converted into a peak-and-peak pattern for the controlled case $f_e/f_o = 3.33$ (see figures 13*d*–13*f*). The symmetric shedding mode of the wake vortex weakens the interactions between the upper and lower wake vortices, resulting in the reduction of the transverse Reynolds normal stresses. Their peaks also move upstream near $x/D = 1.5$, where the induced wake vortex nearly forms and starts to separate from the shear layer.

The distributions of the time-averaged Reynolds shear stresses $\overline{\tilde{u}\tilde{v}}$, $\overline{\hat{u}\hat{v}}$ and $\overline{u'v'}$ are nearly the same for the natural case (see figures 14*a*–14*c*). They are all antisymmetric about the x-axis, with the peaks located near $x/D = 2.8$. For $f_e/f_o = 3.33$ (see figures 14*d*–14*f*), the distributions of $\overline{\tilde{u}\tilde{v}}$, $\overline{\hat{u}\hat{v}}$ and $\overline{u'v'}$ are also antisymmetric about

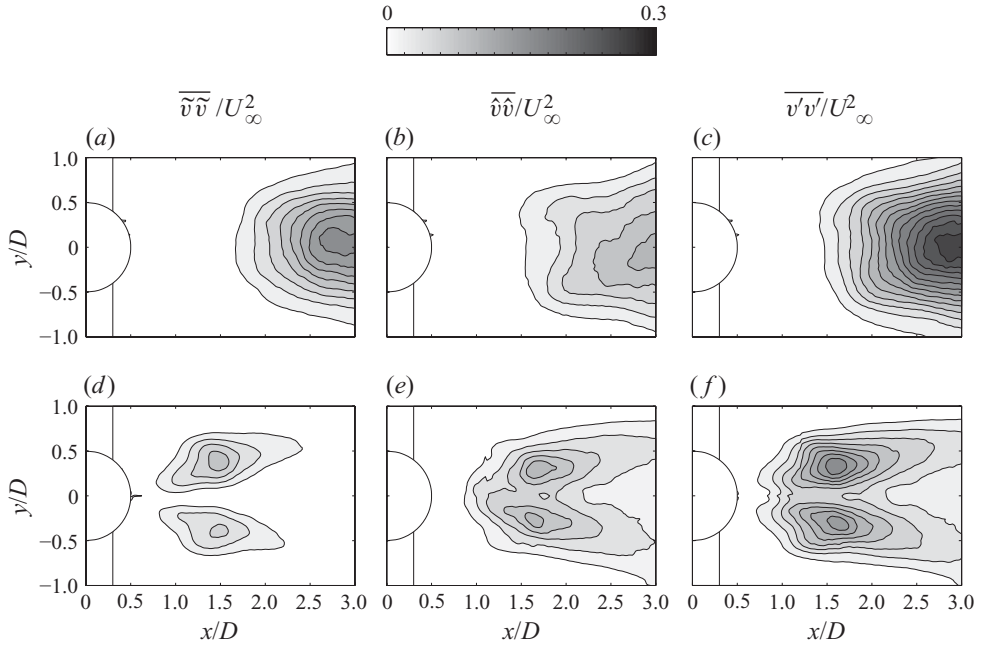

FIGURE 13. Time-averaged transverse Reynolds normal stresses: $\overline{\tilde{v}\tilde{v}}/U_\infty^2$, $\overline{\hat{v}\hat{v}}/U_\infty^2$ and $\overline{v'v'}/U_\infty^2$ for the natural (*a–c*) and $f_e/f_o = 3.33$ (*d–f*) cases. Contour levels: 0.02.

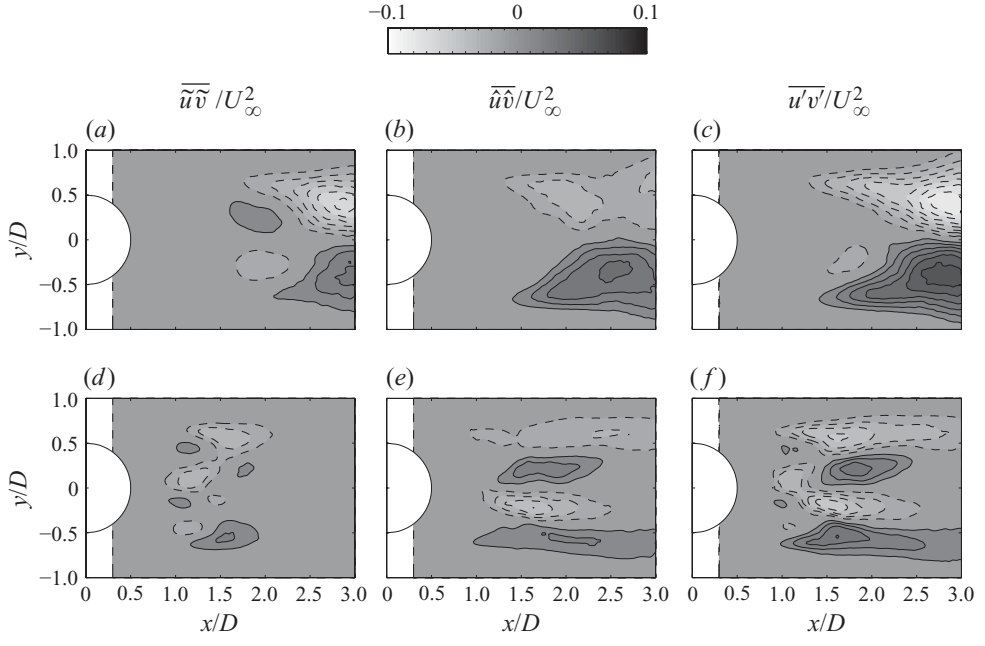

FIGURE 14. Time-averaged Reynolds shear stresses: $\overline{\tilde{u}\tilde{v}}/U_\infty^2$, $\overline{\hat{u}\hat{v}}/U_\infty^2$ and $\overline{u'v'}/U_\infty^2$ for the natural (*a–c*) and $f_e/f_o = 3.33$ (*d–f*) cases. Contour levels: ± 0.01.

the x-axis, while the distribution patterns change evidently compared with the natural case. The peak Reynolds shear stresses are reduced, since the interactions between the upper and lower wake vortices are weakened due to the symmetric shedding mode.

Natural case	*Re*	$\overline{\tilde{u}\tilde{u}}$	$\overline{\hat{u}\hat{u}}$	$\overline{u'u'}$	$\overline{\tilde{v}\tilde{v}}$	$\overline{\hat{v}\hat{v}}$	$\overline{v'v'}$	$\overline{\tilde{u}\tilde{v}}$	$\overline{\hat{u}\hat{v}}$	$\overline{u'v'}$
Cantwell & Coles (1983)	140 000	0.08	–	0.22	0.23	–	0.43	0.05	–	0.12
		36 %	–	100 %	53 %	–	100 %	42 %	–	100 %
Govardhan & Williamson	3900	0.065	–	0.11	0.18	–	0.23	0.06	–	0.085
(2001)		59 %	–	100 %	78 %	–	100 %	71 %	–	100 %
Konstantinidis *et al*.	2160	0.07	–	0.15	0.28	–	0.32	0.08	–	0.09
(2005*b*)		47 %	–	100 %	88 %	–	100 %	89 %	–	100 %
Kim *et al*. (2006)	360	0.14	–	0.18	0.34	–	0.38	0.08	–	0.10
		78 %	–	100 %	89 %	–	100 %	80 %	–	100 %
Konstantinidis & Balabani	2150	0.12	–	0.16	0.29	–	0.33	0.08	–	0.09
(2008)		75 %	–	100 %	88 %	–	100 %	89 %	–	100 %
This study	950	0.060	0.080	0.11	0.17	0.11	0.27	0.065	0.046	0.079
		55 %	73 %	100 %	63 %	41 %	100 %	82 %	58 %	100 %
Controlled case	*Re*	$\overline{\tilde{u}\tilde{u}}$	$\overline{\hat{u}\hat{u}}$	$\overline{u'u'}$	$\overline{\tilde{v}\tilde{v}}$	$\overline{\hat{v}\hat{v}}$	$\overline{v'v'}$	$\overline{\tilde{u}\tilde{v}}$	$\overline{\hat{u}\hat{v}}$	$\overline{u'v'}$
Konstantinidis *et al*.	2160	0.27	–	0.31	0.64	–	0.66	0.16	–	0.16
(2005*b*)		87 %	–	100 %	97 %	–	100 %	100 %	–	100 %
Kim *et al*. (2006)	360	0.24	–	0.29	0.47	–	0.52	0.12	–	0.13
		83 %	–	100 %	90 %	–	100 %	92 %	–	100 %
Konstantinidis & Balabani	2150	0.25	–	0.31	0.52	–	0.60	0.14	–	0.16
(2008)		81 %	–	100 %	87 %	–	100 %	88 %	–	100 %
This study, $f_e/f_o = 1.67$	950	0.053	0.094	0.095	0.029	0.12	0.12	0.024	0.057	0.058
		56 %	99 %	100 %	24 %	100 %	100 %	41 %	98 %	100 %
This study, $f_e/f_o = 2.50$	950	0.069	0.093	0.13	0.034	0.072	0.096	0.016	0.035	0.039
		53 %	72 %	100 %	35 %	75 %	100 %	41 %	90 %	100 %
This study, $f_e/f_o = 3.33$	950	0.093	0.13	0.18	0.090	0.11	0.18	0.029	0.040	0.048
		52 %	72 %	100 %	50 %	61 %	100 %	60 %	83 %	100 %
This study, $f_e/f_o = 5.00$	950	0.19	0.21	0.34	0.15	0.19	0.31	0.054	0.066	0.094
		55 %	62 %	100 %	48 %	61 %	100 %	57 %	70 %	100 %

TABLE 2. Peak coherent, incoherent and total Reynolds stresses and their percentages of the total component peak values at $Re = 950$ for the natural and $f_e/f_o = 1.67$, 2.50, 3.33 and 5.50 cases of the present paper. Related results at different Reynolds numbers from other researchers are also listed for the comparison (Cantwell & Coles 1983; Govardhan & Williamson 2001; Konstantinidis *et al.* 2005*b*; Kim *et al.* 2006; Konstantinidis & Balabani 2008).

Table 2 summarizes the maxima of the coherent, incoherent and total Reynolds stresses and their percentages of the total component peak values. The present results are also compared with the previous investigations from Cantwell & Coles (1983), Govardhan & Williamson (2001), Konstantinidis *et al.* (2005*b*), Kim *et al.* (2006) and Konstantinidis & Balabani (2008). It is indicated that the present results for the natural case are very similar to Govardhan & Williamson's (2001) results. For the vortex-synchronization cases, the maximum of $\overline{u'u'}$ decreases by 14 % for $f_e/f_o = 1.67$. Then it increases with the excitation frequency and reaches a maximum by 200 % for $f_e/f_o = 5.00$. The maxima of the coherent and incoherent streamwise components have a similar variation. However, the percentage of the peak coherent streamwise component to the peak total component is nearly unchanged and stays at around 55 %, while that of the incoherent component decreases with the excitation frequency. The variations of $\overline{v'v'}$ and $\overline{u'v'}$ are nearly the same. Their peak values for $1.67 \leqslant f_e/f_o \leqslant 3.33$ are reduced compared with the natural case, with the optimum reduction of about 64 % and 51 %, respectively, at $f_e/f_o = 2.50$. Then the maxima of $\overline{v'v'}$ and $\overline{u'v'}$ increase with the excitation frequency for $2.50 \leqslant f_e/f_o \leqslant 5.00$. The maxima of the coherent and incoherent components have a similar variation to the

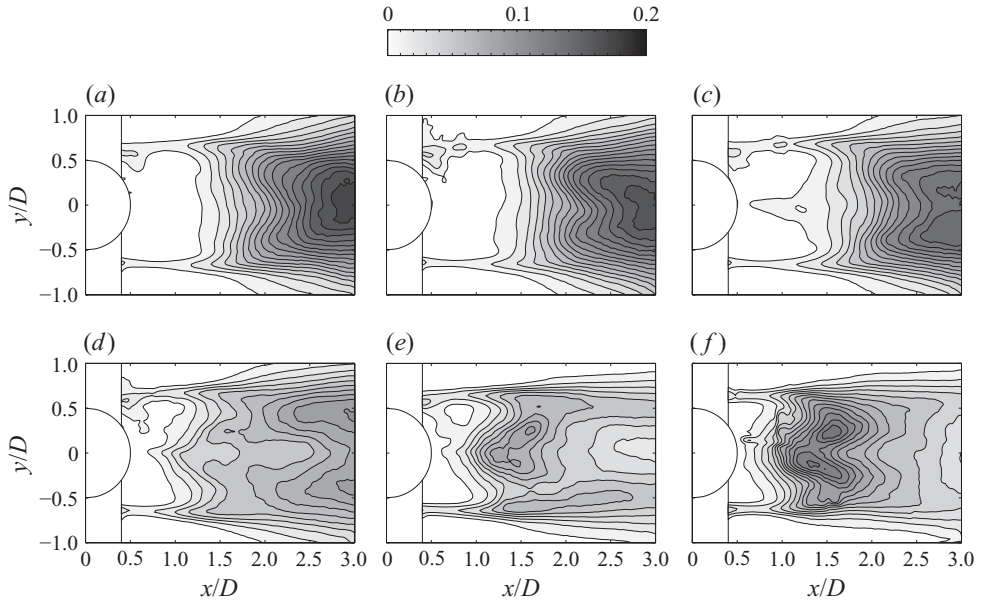

FIGURE 15. TKE. (*a*) Natural; (*b*) $f_e/f_o = 0.50$; (*c*) 0.83; (*d*) 1.67; (*e*) 2.50; (*f*) 3.33. Contour levels: 0.01.

total ones. However, their peak percentages of the peak total component increase and decrease with the excitation frequency, respectively. Konstantinidis *et al.* (2005*b*), Kim *et al.* (2006) and Konstantinidis & Balabani (2008) all indicated that the percentages of the peak coherent component to the total ones increased by means of the streamwise perturbations imposed on the free stream, which are also consistent with the present variation.

The turbulent kinetic energy (TKE), which is defined as $0.5(\overline{u'u'}/U_\infty^2 + \overline{v'v'}/U_\infty^2)$, is associated to the vortex structures and usually used as the measurement of the turbulence mixing (Benard *et al.* 2008; Schäfer, Breuer & Durst 2009). Figure 15 presents distributions of the TKE for the natural and controlled cases. It is suggested that the synthetic jet can enhance the TKE in the near wake for $x/D \leqslant 2$, and the increment is more significant at a higher excitation frequency, whereas the TKE decreases for $x/D \geqslant 2$, and it is much lower as the excitation frequency increases. The production of the TKE can be related to the dynamics of the vortices. For the vortex-synchronization cases, the flow field is dominated by the synthetic-jet vortices, which are located much more upstream near the rear of the circular cylinder. The synthetic jet can thus enhance the turbulence mixing in the near wake. In contrast, the induced wake vortices shed downstream symmetrically with a large distance from each other, resulting in a decrease in their interactions. Thus, the TKE further downstream is reduced.

7. Flow topology

Figure 16 presents the variations of the time-averaged streamwise velocity for both the natural and controlled cases. There exists a large velocity defect in the near-wake region of the circular cylinder due to the flow separation for the natural case (see figure 16*a*). When synthetic jet operates (see figures 16*b*–16*f*), it injects momentum into the near-wake region from the rear stagnation point. Thus, the

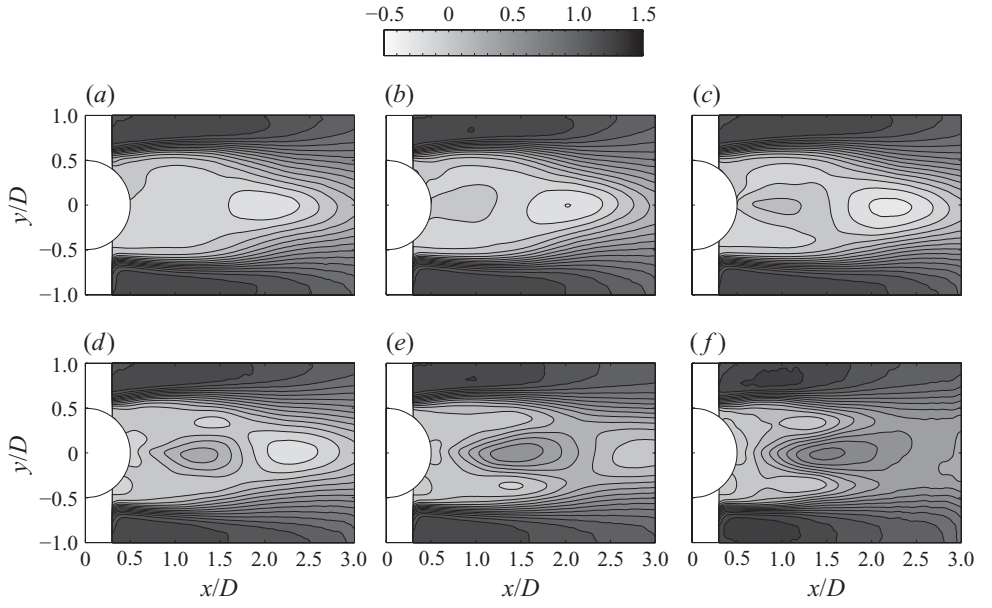

FIGURE 16. Time-averaged streamwise velocity U/U_∞. (*a*) Natural; (*b*) $f_e/f_o = 0.50$; (*c*) 0.83; (*d*) 1.67; (*e*) 2.50; (*f*) 3.33. Contour levels: 0.1.

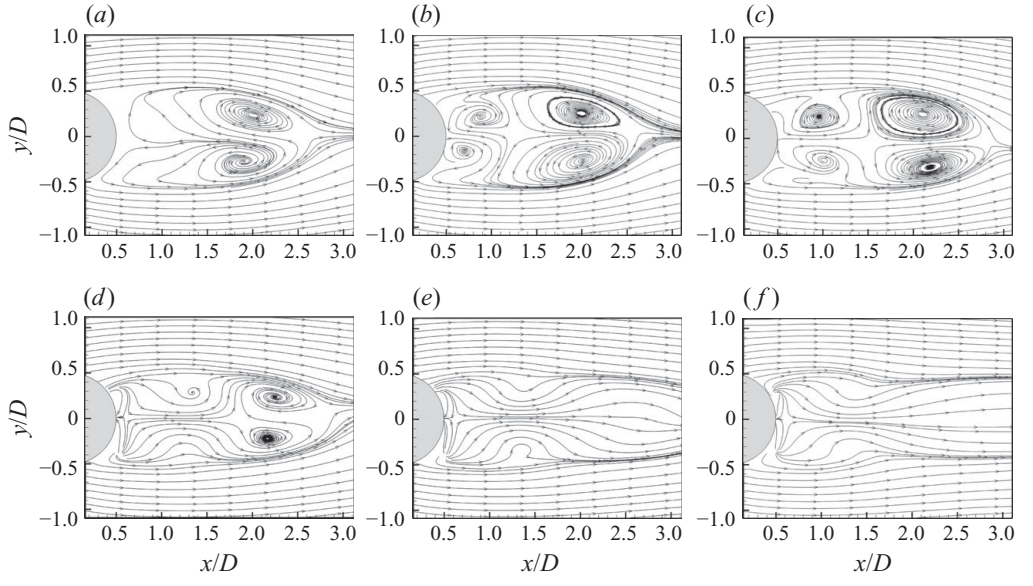

FIGURE 17. Time-averaged streamlines. (*a*) Natural; (*b*) $f_e/f_o = 0.50$; (*c*) 0.83; (*d*) 1.67; (*e*) 2.50; (*f*) 3.33.

streamwise velocity near the rear stagnation point increases, and consequently, the velocity defect decreases as the excitation frequency becomes larger. The backward flow almost disappears in the near wake where it exhibits a jet-flow-like characteristic for $f_e/f_o \geqslant 2.50$.

The time-averaged streamlines are presented in figure 17. Note that the time-averaged streamlines are not completely symmetric about the centreline. This should

be due to the system error during the PIV measurement induced by the limited sample numbers of 100 s as well as some small disturbances that make the synthetic jet travel apart from the centreline. However, the present recorded data are sufficient to illustrate the character of the flow field. It is shown that for the natural case (see figure 17*a*), there is a large recirculation region where the backward flow is obvious behind the circular cylinder. For $f_e/f_o = 0.50$ and $f_e/f_o = 0.83$ (see figures 17*b* and 17*c*), the exit velocity of the synthetic jet is smaller, resulting in the formation of two recirculation regions located upstream and downstream, respectively. The upstream recirculation region is induced by the periodic blowing and suction of the synthetic jet, while the downstream recirculation region forms due to the inherent flow separation of the circular cylinder. The downstream recirculation is smaller than the natural case because of the formation of the upstream recirculation region. The exit velocity for $f_e/f_o = 1.67$ further increases, resulting in the disappearance of the recirculation region near the rear stagnation point and also the reduction of the downstream recirculation region (see figure 17*d*); whereas a new rear stagnation point forms near $x/D = 0.59$. The streamlines upstream of this point are pointing to the rear stagnation point of the circular cylinder. For $f_e/f_o = 2.50$ and $f_e/f_o = 3.33$ (see figures 17*e* and 17*f*), the new stagnation point also forms near $x/D = 0.6$ and the streamlines directing to the exit are more obvious, indicating that the flow separation around the circular cylinder is delayed or even fully attached. The downstream recirculation region completely disappears and exhibits a jet-flow-like characteristic. Therefore, the flow topology of the circular cylinder changes with the synthetic-jet flow control. It is similar to that of Fu & Rockwell (2005) and Baek & Karniadakis (2009), who controlled the cylinder by means of base bleed and also observed two recirculation regions in the near wake due to the effect of the localized rear-stagnation-point jet. The formations of the recirculation region near the rear stagnation point are all a result of the localized jet. However, the difference of the current research is that a periodic zero-net-mass-flux jet was used, while the results of Fu & Rockwell (2005) and Baek & Karniadakis (2009) were based on the steady continuous jet.

8. Summary and discussion

The flow over a circular cylinder is controlled by a two-dimensional synthetic jet positioned at the mean rear stagnation point at the cylinder Reynolds number $Re = 950$. The PIV measurement indicates that the present arrangement can lead to a novel and interesting phenomenon: each synthetic-jet vortex pair could induce a new wake vortex pair with a symmetric shedding mode. We believe that the present finding is innovative and it will further broaden conventional control ideas, especially for the occurrence of the vortex synchronization and the symmetric shedding mode.

The synthetic-jet vortex pairs are induced near the exit by the periodic blowing and suction. Then they convect downstream and interact with the vorticity shear layers behind both sides of the circular cylinder, resulting in the concentration of vorticities near the tails of the shear layers. Eventually, the concentrated vorticities separate from the shear layers and roll up into vortex structures shedding downstream. There exists a one-to-one correspondence between the new induced wake vortex and the synthetic-jet vortex. The circulation, trajectory and convection velocity of the induced wake vortex are all affected by the synthetic-jet vortex pair. Combined with the power-spectral-density analysis, it is indicated that the wake vortex is synchronized by the synthetic jet at the excitation frequency in the range $1.67 \leqslant f_e/f_o \leqslant 5.00$, while it does not occur for $f_e/f_o \leqslant 0.83$, and the transition range $0.83 < f_e/f_o < 1.67$ needs

to be further investigated, when the dimensionless stroke length is fixed at 99.5. The present vortex-synchronization regime is similar to the previous investigations, which are usually around $f_e/f_o = 2$. These data were mostly achieved by the streamwise perturbations imposed on the free-stream velocity when there was a sufficient large periodic component superimposed upon it (Armstrong *et al.* 1986; Barbi *et al.* 1986; Hall & Griffin 1993; Konstantinidis *et al.* 2003; Jarża & Podolski 2004; Kim *et al.* 2006, 2009). The difference is that these investigations usually show vortex synchronization at the subharmonic excitation frequency, namely the actual vortex-shedding frequency is half of the excitation frequency and still in the vicinity of the natural Kármán-vortex-shedding frequency, while vortex synchronization at the excitation frequency is obtained in the present paper.

However, the mechanism for the occurrence of vortex synchronization induced by the rear-stagnation-point perturbations is different from that induced by the perturbations near the separation point. For the latter case, the perturbations can interact with the shear layer directly through the Kelvin–Helmholtz instability, and usually a small perturbation with the natural shedding frequency or its harmonic may trigger the global variations of the wake vortex. The selected frequency plays an important role in the flow control. For the former case, the localized perturbations interact with the wake shear layers though a rear recirculation region and it is the strong shear stress that induces the new wake vortex. Thus, the strength of the synthetic-jet vortex, which is determined by the Reynolds number $Re_{\overline{U_o}}$ based on the time-averaged blowing velocity over one entire cycle, must not be too small to avoid being attenuated in the rear recirculation region before interacting with the wake shear layers. Consequently, the Reynolds number $Re_{\overline{U_o}}$ should be a more crucial factor in determining the interaction between the synthetic jet and the wake vortex rather than the excitation frequency. Knowing this, the excitation frequencies equal to the natural shedding frequency and its harmonics are not particularly selected in this paper, since once the control effects of certain frequencies are determined, other excitation frequencies among them can be easily deduced, regardless of whether they are integer multiples of the unforced frequency. Although this paper considers only one single cylinder Reynolds number, however, based on the present analysis of the control process and control mechanism of the synthetic jet on the cylinder flow, it can be deduced that the synthetic jet will still effectively control flow around a circular cylinder at higher Reynolds numbers. This can be further validated for an extensive range of Reynolds numbers.

The vortex-shedding mode also changes when accompanying the vortex-synchronization phenomenon. It is found that the wake vortex is converted into a symmetric shedding mode from its original antisymmetric mode when vortex synchronization occurs. Previous studies indicated that the symmetric perturbations imposed on the cylinder wake might result in a modification of the vortex-shedding mode from its natural antisymmetric one to a symmetric one (Ongoren & Rockwell 1988; Xu *et al.* 2006; Konstantinidis & Balabani 2007). The present synthetic jet injects momentum downstream from the rear stagnation point, which also imposes symmetric perturbations on the cylinder flow.

The variation of the vortex-shedding mode has a significant influence on the global flow field around the circular cylinder. Increasing the excitation frequency, the synthetic-jet exit velocity and vortex strength increase and the velocity defection in the wake region decreases, resulting in the variations of the flow-field topology: two and one recirculation regions form successively and completely disappear ultimately. Besides, the distributions of the velocity fluctuations and Reynolds stresses also change

essentially when the wake-vortex shedding is converted into a symmetric mode from the original antisymmetric mode; whereas the distributions are still dominated by the large-scale coherent vortex structures, which accords with the four-quadrant-type distribution rule of Balachandar *et al.* (1997). The time-averaged Reynolds stresses show regular changes as the excitation frequency increases. The Reynolds stresses beyond the wake region are reduced with the peak values moving upstream. This is also similar to the variations of the TKE distribution.

Both Amitay *et al.* (1998) and Fujisawa & Takeda (2003) found that the Reynolds stresses at $x/D = 3$ were decreased, which is in good agreement with the present paper. Amitay *et al.* (1998) indicated that this decrease was the result of enhanced dissipation, which was affected by direct coupling of the excitation to the small-scale motions within the wake region, while Fujisawa & Takeda (2003) suggested that the smaller Reynolds stresses in the near-wake region were attributed to the smaller gradient behind the cylinder. As can be seen from the present global flow field around the circular cylinder, the variations of the Reynolds stresses with the excitation frequency reflect the control effect of the synthetic jet. The symmetric shedding mode of the wake vortex weakens the interaction between the upper and lower wake vortices, resulting in the reduction of the produced Reynolds stresses. As the excitation frequency increases, the exit velocity and vorticity strength of the synthetic jet are enhanced and the flow field around the circular cylinder is dominated by the synthetic jet gradually. The Reynolds stresses produced by the synthetic jet are enhanced, while the Reynolds stresses produced by the induced wake vortex are reduced. The moving upstream of the peak Reynolds stresses is related to the position of the maximum circulation of the synthetic-jet vortex and the shortened formation length of the induced wake vortex.

This work has been supported by the National Natural Science Foundation of China (no. 10832001 and no. 50976007). The authors would like to thank Dr T. N. Jukes for his proof-reading of the paper and referees for their valuable comments.

REFERENCES

Akilli, H., Karakus, C., Akar, A., Sahin, B. & Tumen, N. F. 2008 Control of vortex shedding of circular cylinder in shallow water flow using an attached splitter plate. *Trans. ASME J. Fluids Engng* **130**, 041401 (1–11).

Akilli, H., Sahin, B. & Tumen, N. F. 2005 Suppression of vortex shedding of circular cylinder in shallow water by a splitter plate. *Flow Meas. Instrum.* **16**, 211–219.

Amitay, M., Honohan, A., Trautman, M. & Glezer, A. 1997 Modification of the aerodynamic characteristics of bluff bodies using fluidic actuators. *AIAA Paper* 97-2004.

Amitay, M., Smith, B. L. & Glezer, A. 1998 Aerodynamic flow control using synthetic jet technology. *AIAA Paper* 98-0208.

Armstrong, B. J., Barnes, F. H. & Grant, I. 1986 The effect of a perturbation on the flow over a bluff cylinder. *Phys. Fluids* **29**, 2095–2102.

Armstrong, B. J., Barnes, F. H. & Grant, I. 1987 A comparison of the structure of the wake behind a circular cylinder in a steady flow with that in a perturbed flow. *Phys. Fluids* **30**, 19–26.

Baek, H. & Karniadakis, G. E. 2009 Suppressing vortex-induced vibrations via passive means. *J. Fluids Struct.* **25**, 848–866.

Balachandar, S., Mittal, R. & Najjar, F. M. 1997 Properties of the mean recirculation region in the wakes of two-dimensional bluff bodies. *J. Fluid Mech.* **351**, 167–199.

Barbi, C., Favier, D. P., Maresca, C. A. & Telionis, D. P. 1986 Vortex shedding and lock-on of a circular cylinder in oscillatory flow. *J. Fluid Mech.* **170**, 527–544.

Benard, N., Balcon, N., Touchard, G. & Moreau, E. 2008 Control of diffuser jet flow: turbulent kinetic energy and jet spreading enhancements assisted by a non-thermal plasma discharge. *Exp. Fluids* **45**, 333–355.

Bendat, J. S. & Piersol, A. G. 2010 *Random Data: Analysis and Measurement Procedures*. Wiley.

Béra, J. C., Michard, M., Sunyach, M. & Comte-Bellot, G. 2000 Changing lift and drag by jet oscillation: experiments on a circular cylinder with turbulent separation. *Eur. J. Mech.* B/*Fluids* **19**, 575–595.

Blackburn, H. M. & Henderson, R. D. 1999 A study of two-dimensional flow past an oscillating cylinder. *J. Fluid Mech.* **385**, 255–286.

Cantwell, B. & Coles, D. 1983 An experimental study of entrainment and transport in the turbulent near wake of a circular cylinder. *J. Fluid Mech.* **136**, 321–374.

Choi, H., Jeon, W. P. & Kim, J. 2008 Control of flow over a bluff body. *Annu. Rev. Fluid Mech.* **40**, 113–139.

Crook, A., Sadri, A. M. & Wood, N. J. 1999 The development and implementation of synthetic jets for the control of separated flow. *AIAA Paper* 99-3176.

Detemple-Laake, E. & Eckelmann, H. 1989 Phenomenology of Kármán vortex streets in oscillatory flow. *Exp. Fluids* **7**, 217–227.

Dipankar, A., Sengupta, T. K. & Talla, S. B. 2007 Suppression of vortex shedding behind a circular cylinder by another control cylinder at low Reynolds numbers. *J. Fluid Mech.* **573**, 171–190.

Feng, L. H., Wang, J. J. & Xu, C. J. 2008 Experimental verification of a novel actuator signal for efficient synthetic jet (in Chinese). *J. Exp. Fluid Mech.* **22**, 6–10.

Fu, H. & Rockwell, D. 2005 Shallow flow past a cylinder: control of the near wake. *J. Fluid Mech.* **539**, 1–24.

Fujisawa, N. & Takeda, G. 2003 Flow control around a circular cylinder by internal acoustic excitation. *J. Fluids Struct.* **17**, 903–913.

Fujisawa, N., Takeda, G. & Ike, N. 2004 Phase-averaged characteristics of flow around a circular cylinder under acoustic excitation control. *J. Fluids Struct.* **19**, 159–170.

Gau, C., Wu, S. X. & Su, H. S. 2001 Synchronization of vortex shedding and heat transfer enhancement over a heated cylinder oscillating with small amplitude in streamwise direction. *Trans. ASME J. Heat Transfer* **123**, 1139–1148.

Glezer, A. & Amitay, M. 2002 Synthetic jets. *Annu. Rev. Fluid Mech.* **34**, 503–529.

Govardhan, R. & Williamson, C. H. K. 2001 Mean and fluctuating velocity fields in the wake of a freely-vibrating cylinder. *J. Fluids Struct.* **15**, 489–501.

Griffin, O. M. & Hall, M. S. 1991 Review–vortex shedding lock-on and flow control in bluff body wakes. *Trans. ASME J. Fluids Engng* **113**, 526–537.

Griffin, O. M. & Ramberg, S. E. 1976 Vortex shedding from a cylinder vibrating in line with an incident uniform flow. *J. Fluid Mech.* **75**, 257–271.

Hall, M. S. & Griffin, O. M. 1993 Vortex shedding and lock-on in a perturbed flow. *Trans. ASME J. Fluids Engng* **115**, 283–291.

Hall, J. W., Ziada, S. & Weaver, D. S. 2003 Vortex-shedding from single and tandem cylinders in the presence of applied sound. *J. Fluids Struct.* **18**, 741–758.

Huang, X. Y. 1995 Suppression of vortex shedding from a circular cylinder by internal acoustic excitation. *J. Fluids Struct.* **9**, 563–570.

Huang, X. Y. 1996 Feedback control of vortex shedding from a circular cylinder. *Exp. Fluids* **20**, 218–224.

Huang, J. F., Zhou, Y. & Zhou, T. 2006 Three-dimensional wake structure measurement using a modified PIV technique. *Exp. Fluids* **40**, 884–896.

Hwang, J. Y., Yang, K. S. & Sun, S. H. 2003 Reduction of flow-induced forces on a circular cylinder using a detached splitter plate. *Phys. Fluids* **15**, 2433–2436.

Jarża, A. & Podolski, M. 2004 Turbulence structure in the vortex formation region behind a circular cylinder in lock-on conditions. *Eur. J. Mech.* B/*Fluids* **23**, 535–550.

Jauvtis, N. & Williamson, C. H. K. 2004 The effect of two degrees of freedom on vortex-induced vibration at low mass and damping. *J. Fluid Mech.* **509**, 23–62.

Jukes, T. N. & Choi, K. S. 2009 Flow control around a circular cylinder using pulsed dielectric barrier discharge surface plasma. *Phys. Fluids* **21**, 084103.

Jukes, T. N., Choi, K. S., Johnson, G. A. & Scott, S. J. 2006 Turbulent drag reduction by surface plasma through spanwise flow oscillation. *AIAA Paper* 2006-3693.

Kim, S. H., Park, J. Y., Park, N., Bae, J. H. & Yoo, J. Y. 2009 Direct numerical simulation of vortex synchronization due to small perturbations. *J. Fluid Mech.* **634**, 61–90.

Kim, W., Yoo, J. Y. & Sung, J. 2006 Dynamics of vortex lock-on in a perturbed cylinder wake. *Phys. Fluids* **18**, 074103.

Konstantinidis, E. & Balabani, S. 2007 Symmetric vortex shedding in the near wake of a circular cylinder due to streamwise perturbations. *J. Fluids Struct.* **23**, 1047–1063.

Konstantinidis, E. & Balabani, S. 2008 Flow structure in the locked-on wake of a circular cylinder in pulsating flow: effect of forcing amplitude. *Intl J. Heat Fluid Flow* **29**, 1567–1576.

Konstantinidis, E., Balabani, S. & Yianneskis, M. 2003 The effect of flow perturbations on the near wake characteristics of a circular cylinder. *J. Fluids Struct.* **18**, 367–386.

Konstantinidis, E., Balabani, S. & Yianneskis, M. 2005*a* The timing of vortex shedding in a cylinder wake imposed by periodic inflow perturbations. *J. Fluid Mech.* **543**, 45–55.

Konstantinidis, E., Balabani, S. & Yianneskis, M. 2005*b* Conditional averaging of PIV plane wake data using a cross-correlation approach. *Exp. Fluids* **39**, 38–47.

Krishnamoorthy, S., Price, S. J. & Païdoussis, M. P. 2001 Cross-flow past an oscillating circular cylinder: synchronization phenomena in the near wake. *J. Fluids Struct.* **15**, 955–980.

Liu, S. & Fu, S. 2003 Regimes of vortex shedding from an in-line oscillating circular cylinder in the uniform flow. *Acta Mechanica Sin.* **19**, 118–126.

Lucor D. & Karniadakis G. E. 2004 Noisy inflows cause a shedding-mode switching in flow past an oscillating cylinder. *Phys. Rev. Lett.* **92**, 154501.

Mahir, N. & Rockwell, D. 1996 Vortex formation from a forced system of two cylinders. Part I. Tandem arrangement. *J. Fluids Struct.* **10**, 473–489.

Mittal, S. 2003 Effect of a 'slip' splitter plate on vortex shedding from a cylinder. *Phys. Fluids* **15**, 817–820.

Nishihara, T., Kaneko, S. & Watanabe, T. 2005 Characteristics of fluid dynamic forces acting on a circular cylinder oscillated in the streamwise direction and its wake patterns. *J. Fluids Struct.* **20**, 505–518.

Ongoren, A. & Rockwell, D. 1988 Flow structure from an oscillating cylinder. Part 2. Mode competition in the near wake. *J. Fluid Mech.* **191**, 225–245.

Raffel, M., Willert, C. E., Wereley, S. T. & Kompenhans, J. 2007 *Particle Image Velocimetry: A Practical Guide*. Springer.

Reynolds, W. C. & Hussain, A. K. M. F. 1972 The mechanics of an organized wave in turbulent shear flow. Part 3. Theoretical models and comparisons with experiments. *J. Fluid Mech.* **54**, 263–288.

Schäfer, F., Breuer, M. & Durst, F. 2009 The dynamics of the transitional flow over a backward-facing step. *J. Fluid Mech.* **623**, 85–119.

Shuster, J. M. & Smith, D. R. 2007 Experimental study of the formation and scaling of a round synthetic jet. *Phys. Fluids* **19**, 045109.

Smith, B. L. & Glezer, A. 1998 The formation and evolution of synthetic jets. *Phys. Fluids* **10**, 2281–2297.

Stansby, P. K. 1976 The locking-on of vortex shedding due to the cross-stream vibration of circular cylinders in uniform and shear flows. *J. Fluid Mech.* **74**, 641–665.

Sung, J. & Yoo, J. Y. 2003 Near-wake vortex motions behind a circular cylinder at low Reynolds number. *J. Fluids Struct.* **17**, 261–274.

Szepessy, S., & Bearman, P. W. 1992 Aspect ratio and end plate effects on vortex shedding from a circular cylinder. *J. Fluid Mech.* **234**, 191–217.

Tan, G. K., Wang, J. J. & Li, Q. S. 2001 Drag reduction technique of cylinder and mechanism research (in Chinese). *J. Beijing Univ. Aero. Astro.* **27**, 658–661.

Tensi, J., Boué, I., Paillé, F. & Dury, G. 2002 Modification of the wake behind a circular cylinder by using synthetic jets. *J. Visual.* **5**, 37–44.

Wang, J. J., Feng, L. H. & Xu, C. J. 2007 Experimental investigations on separation control and flow structure around a circular cylinder with synthetic jet. *Sci. China, Ser.* E **50**, 550–559.

Xu, S. J., Zhou, Y. & Wang, M. H. 2006 A symmetric binary-vortex street behind a longitudinally oscillating cylinder. *J. Fluid Mech.* **556**, 27–43.

Zdravkovich, M. M. 1997 *Flow Around Circular Cylinders*, vol. 1, *Fundamentals*. Oxford University Press.

Zhang, P. F., Wang, J. J. & Feng, L. H. 2008 Review of zero-net-mass-flux jet and its application in separation flow control. *Sci. China, Ser.* E **51**, 1315–1344.

Zhou, C. Y. & Graham, J. M. R. 2000 A numerical study of cylinders in waves and currents. *J. Fluids Struct*. **14**, 403–428.

Zhou, Y. & Yiu, M. W. 2006 Flow structure, momentum and heat transport in a two-tandem-cylinder wake. *J. Fluid Mech.* **548**, 17–48.

Zhou, Y., Zhang, H. J. & Yiu, M. W. 2002 The turbulent wake of two side-by-side circular cylinders. *J. Fluid Mech.* **458**, 303–332.